

# Application of a Correspondence Principle to the Free Vibrations of Some Viscoelastic Solids

R.C.Y. Chin  
G.W. Hedstrom  
G. Majda

This paper was published in the  
*Geophysical Journal/Royal Astronomical Society*  
Volume 86, pages 137-166

October 23, 1985



This is a preprint of a paper intended for publication in a journal or proceedings. Since changes may be made before publication, this preprint is made available with the understanding that it will not be cited or reproduced without the permission of the author.

#### DISCLAIMER

This document was prepared as an account of work sponsored by an agency of the United States Government. Neither the United States Government nor the University of California nor any of their employees, makes any warranty, express or implied, or assumes any legal liability or responsibility for the accuracy, completeness, or usefulness of any information, apparatus, product, or process disclosed, or represents that its use would not infringe privately owned rights. Reference herein to any specific commercial product, process, or service by trade name, trademark, manufacturer, or otherwise, does not necessarily constitute or imply its endorsement, recommendation, or favoring by the United States Government or the University of California. The views and opinions of authors expressed herein do not necessarily state or reflect those of the United States Government or the University of California, and shall not be used for advertising or product endorsement purposes.

# Application of a Correspondence Principle to the Free Vibrations of Some Viscoelastic Solids

by

R. C. Y. Chin and G. W. Hedstrom

Lawrence Livermore National Laboratory  
P. O. Box 808, Livermore, California 94550

and G. Majda

Division of Applied Mathematics, Brown University  
Providence, Rhode Island 02912

**Summary.** In this study we apply the correspondence principle for free vibrations of a homogeneous viscoelastic solid derived by Fisher and Leitman to obtain the torsional modes of a homogeneous viscoelastic rod. We also extend the correspondence principle, showing that it may be used to find the frequencies of Love waves in a stratified viscoelastic medium. Finally, we apply the correspondence principle to four viscoelastic materials: the Kelvin-Voigt solid, the Maxwell solid, the standard linear solid, and the Achenbach-Chao solid. We show that in each of these cases some care must be used in applying the correspondence principle because of the presence of multiple solutions. We also examine measures of dissipation of the free vibrations, and we determine the conditions under which the logarithmic decrement may be approximated by the process-independent  $1/Q$  of O'Connell and Budiansky.

## 1 Introduction

In this study we are concerned with some problems in viscoelastic wave propagation. Viscoelastic media are of geophysical interest because Spencer (1981) has found that they model fully saturated porous rocks. In addition, the experiments of Bonner (reported in (Thigpen *et al.* 1983)) show that a partially melted granitic rock is modelled by a viscoelastic material. An understanding of wave propagation processes in fully or partially saturated porous materials is basic to energy resource recovery, geothermal exploration, and resource assessment. In addition, in solid earth geophysics the study of attenuation and dispersion of seismic waves involves the theory of linear viscoelasticity. In particular, the damping of the free oscillations of the earth, i. e., the quality factor  $Q$  is a topic of considerable interest. The aim of this study is to increase our understanding of viscoelastic wave propagation with a view toward applications in the analysis of attenuation and dispersion in geophysical materials.

For the elastic wave equation consider solutions of the form of sinusoidal waves  $U(\mathbf{x})\exp(i\omega_0 t)$ . Then the amplitude  $U$  of the displacement field satisfies a differential equation which is formally self-adjoint (Achenbach 1975), and the frequency  $\omega_0$  is an eigenvalue. Thus, if the problem is on a bounded domain with Dirichlet, Neumann, or Robin boundary conditions, the problem as a whole is self-adjoint and the eigenvalues are real and the spectrum has no continuous component. If, on the other hand, the domain is unbounded and the Sommerfeld radiation condition is used on part of the boundary, then the problem as a

whole is not self-adjoint, so that the spectrum may have one or more continuous components. Even in this case, though, the discrete spectrum is strictly real.

For wave propagation in a viscoelastic medium and sinusoidal solutions  $U(\mathbf{x})\exp(i\omega_\nu t)$  the differential equation for the amplitude  $U$  is not formally self-adjoint. Therefore, even on a bounded domain it remains to be investigated whether the eigenfunctions of the viscoelastic wave operator are complete. See (Naimark 1968, Appendix II) for a discussion of the spectral representation for a non-self-adjoint problem in quantum mechanics. Furthermore, the discrete eigenvalues  $\omega_\nu$  need not be real. For realistic viscoelastic models in which the time-domain creep relaxation function is strictly real, the discrete eigenvalues appear in pairs,

$$\omega_\nu = \pm \mu + ib$$

with  $\mu > 0$  and  $b > 0$ . It should also be noted that for a viscoelastic wave problem in an unbounded domain the Sommerfeld radiation condition must be recast in terms of a projection onto the subspace of outgoing viscoelastic waves.

Starting from a known solution for the motion of an elastic material, there are two standard methods for analyzing wave motion in a corresponding viscoelastic medium. One method is by perturbation from an elastic material to a nearby viscoelastic material. This has been done by several authors, and a careful analysis of the method was given by Majda *et al.* (1985), based on perturbation theory for linear operators (Kato 1966). They found that the validity of the procedure of perturbing elastic modes to obtain viscoelastic modes is highly model dependent. Furthermore, the size of perturbation permitted depends on the frequency and is limited by the distances separating modes. Other than the need to keep eigenvalues separated, the method gives no insight into the reasons for the restrictions.

The other method of analysis is based on the correspondence principle of Fisher & Leitman (1966). This principle says that for simple free vibrations of a homogeneous medium the displacement field  $U(\mathbf{x})\exp(i\omega_\nu t)$  of a viscoelastic solid is related to the elastic displacement field  $U(\mathbf{x})\exp(i\omega_e t)$  according to the conditions that the viscoelastic vibration frequency  $\omega_\nu$  and the corresponding elastic frequency  $\omega_e$  be related by the condition

$$\frac{\omega_\nu}{\omega_e} = \frac{K_\nu}{K_e}, \quad (1.1)$$

where  $K_\nu$  is the complex wave velocity and  $K_e$  is the corresponding real elastic wave velocity. That is, in terms of the elastic modulus  $M_e$  and the density  $\rho$ , we have  $K_e = \sqrt{M_e}/\rho$ . The viscoelastic wave speed  $K_\nu = \sqrt{M_\nu(\omega_\nu)}/\rho$ , depends on the frequency  $\omega_\nu$ , and it is complex, because the viscoelastic material modulus  $M_\nu$  is complex. The correspondence principle of Fisher and Leitman says nothing about what happens to the continuous part of the spectrum for the elastic problem and it gives no information about completeness of the eigenfunctions in the viscoelastic case. It should be noted that if (1.1) is regarded as a mapping from  $\omega_e$  to  $\omega_\nu$ , there may be more than one branch, and we have to use additional physical principles to select the proper branch.

In this paper we apply the correspondence principle (1.1) of Fisher & Leitman (1966) to the torsional modes of a viscoelastic rod and to viscoelastic Love waves in a stratified medium. In the case of Love waves this is actually an extension of the theory because we remove the restriction that the medium be homogeneous. The motivation for studying these two problems is that we can observe Love waves on seismograms and we can do laboratory experiments on rods. The theory presented here is needed as background information in the interpretation of the results. For this reason we find the location of the discrete spectrum

for four different viscoelastic materials: a Kelvin-Voigt solid (Leitman & Fisher 1973), a Maxwell solid (Leitman & Fisher 1973), a standard linear solid (Leitman & Fisher 1973), and an Achenbach-Chao model solid (Achenbach & Chao 1962). We show that for each of these solids Eq. (1.1), regarded as an equation for  $\omega_v$ , requires the introduction of a Riemann surface of at least two sheets. We use our knowledge of the high- and low-frequency behavior of the spectrum to identify the principal sheet. The structure of the sheets determines the location of branch cuts joining them. The corresponding branch points form natural barriers for a perturbation expansion. It seems quite possible that the branch cuts may give rise to components of continuous spectrum which have no analogue in the elastic medium. It happens also that for the Achenbach-Chao model solid for a range of values of the parameter, we must introduce still another branch cut because it is impossible to find a single sheet with both the proper high- and low-frequency behavior of the spectrum. A discussion the completeness of the eigenfunctions and the presence of a continuous spectrum is more easily carried out from an analysis of the solution of a dynamic problem in terms of an inverse Laplace transform. We delay such a study to a future paper.

Finally, in Section 4 we examine measures of dissipativity of the free vibrations found in Section 3. We find that the process-independent  $Q$  of O'Connell & Budiansky (1978) is a valid measure of the dissipation only when the dissipation rate is small relative to the frequency of oscillation.

## 2 The Correspondence Principle for Simple Free Vibrations

In this section we apply the correspondence principle (1.1) to obtain the torsional modes of a viscoelastic rod. We then show that in a stratified viscoelastic medium in which the anelasticity depends on depth in a certain special way, the correspondence principle (1.1) may be extended to the modes for Love waves.

The torsional modes for an elastic rod may be determined as given by Achenbach (1975). Let the rod have radius  $r_0$ , and let  $J_j(z)$ ,  $j = 0, 1$ , denote the Bessel function of the first kind and of order  $j$ . Let  $q$  be a solution of the frequency equation,

$$(qr_0)J_0(qr_0) - 2J_1(qr_0) = 0. \quad (2.1)$$

Then in terms of the wave number  $k$  (a real number), the density  $\rho$ , and the elastic modulus  $M_e$ , the corresponding torsional frequency is given by

$$\omega_e = \beta \sqrt{q^2 + k^2}$$

with

$$\beta^2 = M_e / \rho.$$

In terms of the radial position  $r$ , the distance  $z$  along the rod, and the time  $t$ , the elastic displacement field  $v_e$  is given by

$$v_e(r, z, t) = \frac{1}{q} J_1(qr) \exp\{i(kz - \omega_e t)\}.$$

Accordingly, the viscoelastic torsional modes are obtained by solving (1.1) for  $\omega_v$ , and the associated displacement field  $v_v$  is

$$v_v(r, z, t) = \frac{1}{q} J_1(qr) \exp\{i(kz - \omega_v t)\}.$$

For the viscoelastic Love wave problem in a stratified medium, we have from Majda *et al.* (1985) that

$$\frac{d}{dz} \left[ M_v(z, \omega_v) \frac{dv_v}{dz} \right] + [\omega_v^2 \rho(z) - k^2 M_v(z, \omega_v)] v_v = 0, \quad 0 < z < \infty, \quad (2.2)$$

$$\frac{dv_v(0)}{dz} = 0 \quad \text{and} \quad \lim_{z \rightarrow \infty} v_v(z) = 0,$$

where  $k$  is real,  $M_v(z, \omega_v)$  is the depth-dependent complex shear modulus, and  $\rho(z)$  is the density. In (Majda *et al.* 1985) it was assumed that the complex shear modulus varies continuously with  $z$ , but the dependence on  $\omega$  is quite general, provided that  $|M_v - M_e|$  is sufficiently small. Here, we permit  $M_v$  and  $M_e$  to be piecewise continuous in  $z$ , but we impose the condition that the complex shear modulus  $M_v(z, \omega_v)$  be related to the real shear modulus  $M_e(z)$  in the special way,

$$M_v(z, \omega_v) = M_e(z) A(\omega_v), \quad (2.3)$$

where  $A$  is an analytic function. Then a correspondence principle for the stratified Love wave problem may be obtained as follows. We rewrite (2.2) using (2.3) to yield

$$\frac{d}{dz} \left[ M_e(z) \frac{dv_v}{dz} \right] + \left[ \frac{\omega_v^2}{A(\omega_v)} \rho(z) - k^2 M_e(z) \right] v_v = 0. \quad (2.4)$$

The corresponding elastic Love wave equation is

$$\frac{d}{dz} \left[ M_e(z) \frac{dv_e}{dz} \right] + [\omega_e^2 \rho(z) - k^2 M_e(z)] v_e = 0. \quad (2.5)$$

Upon comparing (2.4) with (2.5), we conclude that if  $v_e$  is a mode for the elastic Love wave problem, then it is also a mode for the viscoelastic Love wave problem,  $v_v = v_e$ , and the frequencies are related by

$$\frac{\omega_v^2}{A(\omega_v)} = \omega_e^2. \quad (2.6)$$

The multiplicative decomposition postulate (2.3) restricts the frequency-dependent aspect of the material properties to be independent of depth. This assumption may not be valid for solid earth geophysical applications. It may, however, be a sufficiently good approximation for regional studies.

We remark that this analysis may easily be extended to the case in which the density  $\rho_v$  for the viscoelastic solid is a constant multiple of the corresponding density  $\rho_e$  for the elastic problem. That is, we could just as well let

$$\rho_v(z) = b_v \tilde{\rho}(z), \quad \rho_e(z) = b_e \tilde{\rho}(z),$$

where  $\tilde{\rho}(z)$  is a normalized, dimensionless density and  $b_v$  and  $b_e$  are constants. This change merely causes the introduction of a scaling factor in (2.6).

The correspondence principle reduces the problem of calculating the viscoelastic free vibrations to a study of conformal transformations between complex planes, given by (1.1) for a homogeneous material and by (2.6) for the stratified Love wave problem. In fact, with the notation

$$s = i\omega_v,$$

Eq. (2.6) takes the form

$$f(s) = s \sqrt{\frac{1}{A(-is)}} = i\omega_e. \quad (2.7)$$

In (2.7) it is advantageous to continue  $\omega_e$  onto the complex plane. Thus, we regard  $f(s)$  as a map from the complex  $s$ -plane into the complex  $\omega_e$ -plane. Since the elastic modes  $\omega_e$  are strictly real and are presumed known, it is the inverse transformation  $f^{-1}$  that is of interest. In particular, the correspondence principle amounts to finding the curve  $\Gamma$  in the  $s$ -plane, which is the image of the real line in the  $\omega_e$ -plane. In subsequent sections we determine  $\Gamma$  for a Kelvin-Voigt solid, a Maxwell solid, a Standard Linear solid and an Achenbach-Chao model solid. The mapping  $f^{-1}$  in each case is multivalued. We shall see that the branch points of the multivalued map play an important role.

The complex moduli for these model solids are determined from the constitutive equation. Different viscoelastic models are obtained, depending on the particular constitutive relation, describing the relationship between the stress  $\sigma$  and the strain  $\varepsilon$ . In the next section we display the form of the correspondence principle for four different viscoelastic models.

### 3 The correspondence principle for four viscoelastic models

For four different viscoelastic models  $A(-is)$  we show in this section what values of  $s$  correspond under (2.7) to real elastic modes  $\omega_e$ . In this way we obtain a correspondence principle for Love waves for the Kelvin-Voigt, Maxwell, and Achenbach-Chao model solids and for the standard linear solid. For each of these models the principal results are summarized here and the mathematical details are found in the appendices.

For a *Kelvin-Voigt solid* (Leitman & Fisher 1973) we have

$$\sigma = M_E \left[ \tau_e \frac{\partial \varepsilon}{\partial t} + \varepsilon \right], \quad (3.1)$$

where  $M_E$  is the equilibrium modulus and  $\tau_e$  is the strain relaxation time. Thus, by taking a Laplace transform with respect to  $t$ , we find that for a Kelvin-Voigt solid  $A(-is)$  in (2.7) takes the form

$$A(-is) = \tau_e s + 1. \quad (3.2)$$

Upon introducing the dimensionless variables

$$p = \tau_e s \quad \text{and} \quad \zeta = \frac{\tau_e \omega_e}{2}$$

into (3.2), we obtain for the correspondence relation (2.7)

$$\frac{-ip}{2\sqrt{1+p}} = \zeta. \quad (3.3)$$

Note that if we square (3.3) and clear fractions, we obtain a quadratic equation in  $p$ . Thus, the inverse mapping to (3.3) requires two sheets in the  $p$ -plane. Real values for the elastic modes  $\omega_e$  give real values of  $\zeta$ , and the corresponding values of  $p$  are shown in Fig. 1. Here, the physical branch is drawn as a solid curve and the extraneous branch is drawn with dashes.

Let us return to the physical variables. For  $0 \leq \omega_e \leq 2/\tau_e$  we introduce the auxiliary variable

$$\vartheta = \sin^{-1} \left[ \frac{\tau_e \omega_e}{2} \right]$$

Then, it is shown in Appendix A that the corresponding viscoelastic frequencies of a Kelvin-Voigt solid lie on the circle,

$$\omega_v = \frac{i}{\tau_\varepsilon} (1 - e^{2i\vartheta}). \quad (3.4)$$

Similarly, for  $\omega_\varepsilon > 2/\tau_\varepsilon$  we introduce the auxiliary variable

$$\vartheta = \cosh^{-1} \left[ \frac{\tau_\varepsilon \omega_\varepsilon}{2} \right],$$

and the corresponding viscoelastic frequencies of a Kelvin-Voigt solid lie on the positive imaginary axis,

$$\omega_v = \frac{i}{\tau_\varepsilon} (e^{2\vartheta} + 1). \quad (3.5)$$

In the paper of Majda *et al.* (1985) a perturbation method was used to obtain a correspondence principle for free vibrations of a Kelvin-Voigt solid. Their method used a power series in  $\zeta$  and was shown to be valid for values of  $|\zeta|$  sufficiently small. They obtain a Maclaurin series in  $\zeta$  for the right-hand side of (3.4). We show in the appendix that there are branch points at  $\zeta = \pm 1$ , which act as natural barriers for the circle of convergence of such an expansion.

The viscoelastic modes of a Kelvin-Voigt solid are analogous to the motions of a damped oscillator, in that, (3.4) represents an underdamped oscillation and (3.5) is a overdamped motion. Critical damping occurs at  $\omega_\varepsilon = 2/\tau_\varepsilon$  or  $\zeta = 1$  (the branch point). This overdamped motion is expected since the high-frequency response of a Kelvin-Voigt solid is strictly diffusive. That is, from the point of view of the governing partial differential equations, the system is parabolic in the sense of Petrovsky (Gelfand & Shilov 1967, p. 112).

For a *Maxwell solid* (Leitman & Fisher 1973) the constitutive relation is

$$\frac{\partial \sigma}{\partial t} + \frac{\sigma}{\tau_\sigma} = M_I \frac{\partial \varepsilon}{\partial t},$$

where  $\tau_\sigma$  is the strain relaxation time. Thus, for a Maxwell solid we have

$$A(-is) = \frac{s}{s + \frac{1}{\tau_\sigma}}. \quad (3.6)$$

In terms of the dimensionless variables

$$p = \tau_\sigma s \quad \text{and} \quad \zeta = 2\tau_\sigma \omega_\varepsilon,$$

the correspondence relation (2.7) takes the form

$$-2i\sqrt{p(p+1)} = \zeta. \quad (3.7)$$

Upon squaring (3.7) we again obtain a quadratic equation in  $p$ , so that there are two branches. The values of  $p$  corresponding to real modes  $\omega_\varepsilon$  (and to real  $\zeta$ ) are shown in Fig. 2. Again, the physical branch is drawn with a solid curve, and the extraneous branch is drawn with dashes.

In terms of the physical variables it is shown in Appendix B that for  $0 \leq \omega_\varepsilon \leq 1/(2\tau_\sigma)$  the viscoelastic frequencies of a Maxwell solid are given by

$$\omega_v = \frac{i}{2\tau_\sigma} \left[ 1 - \sqrt{1 - (2\tau_\sigma \omega_\varepsilon)^2} \right]. \quad (3.8)$$

Similarly, for  $\omega_\varepsilon > 1/(2\tau_\sigma)$  the viscoelastic modes of a Maxwell solid are given by

$$\omega_v = \frac{1}{2\tau_\sigma} \left[ i + \sqrt{(2\tau_\sigma \omega_\varepsilon)^2 - 1} \right]. \quad (3.9)$$



Let us again show the connection between our result and the perturbation expansion of Majda *et al.* (1985) for the Maxwell solid. Their expansion is in terms of powers on  $1/\zeta$ , so that it amounts to a Laurent expansion of (3.9) about  $\zeta=\infty$ . It is clear from (3.9) that there are branch points at  $\zeta=\pm 1$ , so that the domain of convergence of such a series is the set  $|\zeta|>1$ .

It is interesting to note that the Maxwell solid doesn't have the low-frequency, weakly damped free vibrations of the Kelvin-Voigt solid. In the Maxwell solid, there are two distinct sets of vibrations, namely, an oscillatory motion with a fixed decay rate (3.9), separated by a critically damped state from a strictly decaying motion (3.8).

For a *standard linear solid* (Leitman & Fisher 1973) the constitutive relation is

$$\frac{\partial \sigma}{\partial t} + \frac{\sigma}{\tau_\sigma} = M_I \left( \frac{\partial \varepsilon}{\partial t} + \frac{\varepsilon}{\tau_\varepsilon} \right)$$

with  $\tau_\sigma < \tau_\varepsilon$ . Thus, for a standard linear solid we have

$$A(-is) = \frac{s + \frac{1}{\tau_\varepsilon}}{s + \frac{1}{\tau_\sigma}}. \quad (3.10)$$

We make a change of variables

$$p = \tau_\sigma s, \quad \zeta = \tau_\sigma \omega_\theta \quad \text{and} \quad a = \frac{\tau_\sigma}{\tau_\varepsilon},$$

and the correspondence principle (2.7) becomes

$$-ip \sqrt{\frac{p+1}{p+a}} = \zeta. \quad (3.11)$$

Upon squaring (3.11) and clearing fractions, we obtain a cubic equation in  $p$ . Consequently, there are two extraneous branches and one physical branch for this viscoelastic model solid.

In Figs. 3–6 the values of  $p$  corresponding to real elastic modes  $\omega_\theta$  are shown for different values of the parameter  $a$ . Again, the physical branches are shown as solid curves, and the extraneous branches are drawn with dashes. In all four of these figures it should be noted that the standard linear solid displays the low-frequency behavior of the Kelvin-Voigt solid and the high-frequency behavior of the Maxwell solid. This phenomenon is most striking for  $a < 1/9$  as in Fig. 3. We show in Appendix C that it is only for  $a < 1/9$  that the standard linear solid displays critical damping and purely decaying motion.

We do not give formulas for  $\omega_\nu$  analogous to (3.8) and (3.9) for the standard linear solid because doing so would require the solution of a cubic equation. We can, however, determine the low- and high-frequency behavior directly from (3.11), and this is done in Appendix C. The low-frequency modes transform according to

$$\omega_\nu = \sqrt{a} \omega_\theta + \frac{i(1-a)}{2} \tau_\sigma \omega_\theta^2 + O(|\omega_\theta|^3) \quad (3.12)$$

as  $\omega_\theta \rightarrow 0$ . The high-frequency modes, on the other hand, transform according to

$$\omega_\nu = \omega_\theta + i \left[ \frac{1-a}{2\tau_\sigma} \right] + O\left(\frac{1}{|\omega_\theta|}\right) \quad (3.13)$$

as  $\omega_\theta \rightarrow \infty$ .

For the standard linear solid Majda *et al.* (1985) obtained an expansion in powers of  $1-a$  for  $p$  as a function of  $\zeta$ , the inverse to (3.11). They showed that this series converges uniformly in  $\zeta$  for  $a$  sufficiently close to 1. We see here that because of the branch point, the value  $a=1/9$  acts as a natural barrier to the domain of convergence of such an expansion.

For an *Achenbach-Chao model solid* (Achenbach & Chao 1962) the constitutive relation is

$$\left( \frac{\partial}{\partial t} + \frac{1}{\tau_\sigma} \right)^2 \sigma = M_I \left( \frac{\partial}{\partial t} + \frac{1}{\tau_\varepsilon} \right)^2 \varepsilon$$

with  $\tau_\sigma < \tau_\varepsilon$ . Thus, for an Achenbach-Chao solid a Laplace transform shows that  $A(-is)$  in (2.7) is given by

$$A(-is) = \left( \frac{\tau_\sigma s + \alpha}{\tau_\sigma s + 1} \right)^2, \quad 0 < \alpha = \frac{\tau_\sigma}{\tau_\varepsilon} < 1. \quad (3.14)$$

In terms of the dimensionless variables

$$p = \tau_\sigma s \quad \text{and} \quad \zeta = \tau_\sigma \omega_\varepsilon / 2$$

with the Achenbach-Chao complex modulus (3.14) the correspondence relation (2.7) takes the form

$$\frac{-ip(p+1)}{2(p+\alpha)} = \zeta \quad (3.15)$$

with  $0 < \alpha < 1$ .

The inverse function to (3.15) is the solution of

$$p^2 + (1 - 2i\zeta)p - 2i\zeta\alpha = 0. \quad (3.16)$$

and is therefore multi-valued, that is, the Riemann surface of  $\zeta$  has two sheets. Consequently, real elastic modes  $\omega_\varepsilon$  become real values of  $\zeta$ , which in turn are mapped by (3.15) onto two branches in the  $p$ -plane. Only for values of  $\alpha$  such that  $0.5 \leq \alpha < 1$  is it possible to identify a physical branch in the  $p$ -plane. The situation is illustrated in Figs. 7–9. In Figs. 8 and 9, in which  $\alpha = 0.5$  and  $0.7$ , it is easy to identify a branch in which the low-frequency behavior is analogous to that of a Kelvin-Voigt solid and the high-frequency behavior is like a Maxwell solid. Note though, that for  $\alpha = 0.5$  in Fig. 8 the physical image meets the extraneous image at the two branch points. For  $\alpha < 0.5$  these curves cross the cut, and it is impossible to obtain the proper high- and low-frequency behavior on a continuous branch. This behavior is shown in Fig. 7 with  $\alpha = 0.3$ . It would be interesting to know the reasons for this phenomenon, but we postpone an investigation to a later study since it would take us too far afield from the purposes of this paper.

We conclude this section with a display of the low- and high-frequency behavior of the modes in terms of the original physical variables. For  $\omega_\varepsilon \rightarrow 0$  we have

$$\omega_\nu = \alpha\omega_\varepsilon + i\alpha(1-\alpha)\tau_\sigma\omega_\varepsilon^2 + O(|\omega_\varepsilon|^3), \quad (3.17)$$

and for  $\omega_\varepsilon \rightarrow \infty$  we have

$$\omega_\nu = \omega_\varepsilon + \frac{(1-\alpha)i}{\tau_\sigma} + O\left(\frac{1}{|\omega_\varepsilon|}\right). \quad (3.18)$$

These formulas are easily obtained from expansions of (3.15) about  $\zeta = 0$  and, respectively, about  $\zeta = \infty$ .

#### 4 A discussion of the decay rate

In this section we compare two measures of the dissipativity of the viscoelastic materials discussed in Section 3, namely, the logarithmic decrement of the oscillatory solutions and the intrinsic "quality" parameter  $Q$  of O'Connell and Budiansky (1978). For a damped periodic oscillation, the logarithmic decrement is a natural measure of the dissipative process, and it is a ratio of two scales, one being the frequency of oscillation and the other the rate of decay of the envelope. The logarithmic decrement is then a dimensionless parameter giving the decay of the motion over one period. Note that the value of the logarithmic decrement depends on the solution of the problem, which in turn depends on the parameters and on the initial and boundary conditions. In particular, the process depends on the history of the solution. The quality factor  $Q$  of O'Connell and Budiansky (1978) depends only on the material parameters, and it is the ratio of the real part to the imaginary part of the complex modulus

$$\frac{1}{Q} = \frac{\text{Im } M(\omega_e)}{\text{Re } M(\omega_e)}, \quad (4.1)$$

for real  $\omega_e$ . We show that  $1/Q$  is a good approximation to the logarithmic decrement when the logarithmic decrement is sufficiently small.

For the viscoelastic free vibrational modes the logarithmic decrement is

$$\frac{1}{2\pi} \ln \Delta = \frac{\text{Im } \omega_v}{\text{Re } \omega_v} \quad (4.2)$$

In terms of the variable  $p = i\tau_e\omega_v$  or  $p = i\tau_\sigma\omega_v$  plotted in Figs. 1–9, this is

$$\frac{1}{2\pi} \ln \Delta = - \frac{\text{Re } p}{\text{Im } p}.$$

Thus, we have

$$\frac{1}{2\pi} \ln \Delta = \tan \vartheta, \quad (4.3)$$

where  $\vartheta$  denotes the angle between the imaginary axis in the  $p$ -plane and the ray from the origin to the point  $p$  in question. For a critically damped or overdamped motion we have  $\vartheta = \pi/2$ , giving an infinite dissipation measure which signifies that the motion is not oscillatory.

We now give the logarithmic decrements for the viscoelastic models studied in Section 3. It follows from Eq. (A.4) in Appendix A that for the Kelvin-Voigt solid with  $0 < \omega_e < 2/\tau_e$  we have (4.3) with

$$\vartheta = \sin^{-1} \left( \frac{\omega_e \tau_e}{2} \right) \quad (4.4)$$

For the Maxwell solid it follows from Eqs. (B.1–3) in Appendix B that for  $\omega_e > 1/2\tau_\sigma$  we have

$$\frac{1}{2\pi} \ln \Delta = \frac{1}{\sqrt{(2\tau_\sigma\omega_e)^2 - 1}}. \quad (4.5)$$

For both the standard linear solid and the Achenbach-Chao model solids, there is no simple formula for the logarithmic decrement. We can, however, obtain its asymptotic behavior for low and high frequencies. Thus, for the standard linear solid it follows from (3.12–13) and from the fact that the coefficient of the cubic term in (3.12) is real that

$$\frac{1}{2\pi} \ln \Delta = \begin{cases} \frac{(1-\alpha)\tau_\sigma \omega_\theta}{2\sqrt{\alpha}} + O(|\omega_\theta|^3) & \text{as } \omega_\theta \rightarrow 0, \\ \frac{(1-\alpha)}{2\tau_\sigma \omega_\theta} + O\left(\frac{1}{|\omega_\theta|^2}\right) & \text{as } \omega_\theta \rightarrow \infty. \end{cases} \quad (4.6)$$

Similarly, for the Achenbach-Chao model solid we see from (3.17–18) that

$$\frac{1}{2\pi} \ln \Delta = \begin{cases} (1-\alpha)\tau_\sigma \omega_\theta + O(|\omega_\theta|^3) & \text{as } \omega_\theta \rightarrow 0, \\ \frac{(1-\alpha)}{\tau_\sigma \omega_\theta} + O\left(\frac{1}{|\omega_\theta|^2}\right) & \text{as } \omega_\theta \rightarrow \infty \end{cases} \quad (4.7)$$

(Here, we have also used the fact that the coefficient of the cubic term in the power series (3.17) is real.)

It should be remembered that for the standard linear solid with  $\alpha \leq 1/9$  there exist values of  $\omega_\theta$  for which the corresponding values of  $p$  are real, so that the motion has no oscillatory component and the logarithmic decrement is infinite. Also, for the Achenbach-Chao solid with  $\alpha < 1/2$ , because of the discontinuity in the viscoelastic spectrum, the logarithmic decrement is discontinuous.

We have seen that for the Kelvin-Voigt solid, the Maxwell solid, and for the standard linear solid with  $\alpha \leq 1/9$ , there exist modes for which there is no period of oscillation with which to compare the decay rate. Thus, to form a dimensionless parameter measuring the dissipation of the process, we would need to compare the decay rate to some characteristic scale of the problem, such as the relaxation rate of the viscoelastic material. In any case we need to make use of the solution which results from the dynamic interactions of the material, geometry, loading process and others. In other words, the dissipation measure will depend on the characteristic parameters of the problem since dissipative processes are path dependent.

In the paper of O'Connell and Budiansky (1978) a correspondence principle was derived between the elastic and the viscoelastic modes. A perturbation analysis was performed to show that for small attenuation in some sense, if the complex modulus is analytic in a neighborhood of the real  $\omega_v$ -line, then all measures of dissipation are equivalent to (4.1). One difficulty with this approach is that it is known from Majda *et al.* (1985) that the choice of a perturbation parameter is model dependent. Another difficulty is that when the dissipation is not small, it may not be possible to measure dissipation with a  $Q$  defined only in terms of the material properties.

In order to investigate these questions for the viscoelastic solids studied in Section 3, we find the  $Q$  using (4.1) and compare it with  $\ln \Delta / (2\pi)$ . Our measure of comparison is the function

$$R = \frac{Q}{\pi} \ln \Delta. \quad (4.8)$$

For the Kelvin-Voigt solid it follows from (3.2) that

$$\frac{1}{Q} = \tau_\epsilon \omega_\theta.$$

Thus, for  $\omega_\theta < 2/\tau_\epsilon$  we see from (4.3) that the function  $R$  defined by (4.8) is given by

$$R = \frac{1}{\sqrt{1 - (\tau_e \omega_e / 2)^2}}. \quad (4.9)$$

Thus,  $R$  becomes singular for the Kelvin-Voigt solid at the frequency at which there is critical damping. Similarly, for the Maxwell solid we obtain from (3.6) that

$$\frac{1}{Q} = \frac{1}{\tau_\sigma \omega_e}.$$

Thus, from (4.5) and (4.8) we have

$$R = \frac{1}{\sqrt{1 - 1/(2\tau_\sigma \omega_e)^2}} \quad (4.10)$$

if  $\omega_e > 1/(2\tau_e)$ . We see that for the Maxwell solid the two measures of dissipation are comparable at high frequencies in the sense that  $R \rightarrow 1$  as  $\omega_e \rightarrow \infty$  but that  $R$  becomes infinite as  $\omega_e$  approaches  $1/(2\tau_e)$ , the largest frequency for which the corresponding viscoelastic motion has no oscillatory component.

For the standard linear solid it follows from (3.10) that

$$\frac{1}{Q} = \frac{(1 - \alpha)\tau_\sigma \omega_e}{\alpha + (\tau_\sigma \omega_e)^2}. \quad (4.11)$$

Thus, for  $\omega_e \rightarrow 0$  we have

$$\frac{1}{Q} = \frac{(1 - \alpha)\tau_\sigma \omega_e}{\alpha} + O(|\omega_e|^3),$$

and upon comparing with (4.6), we obtain

$$R = \sqrt{\alpha} (1 + O(\omega_e^2)).$$

A similar analysis for  $\omega_e \rightarrow \infty$  for the standard linear solid shows that

$$\frac{1}{Q} = \frac{1 - \alpha}{\tau_\sigma \omega_e} \left[ 1 + O\left(\frac{1}{\omega_e^2}\right) \right]$$

and that

$$R = 1 + O\left(\frac{1}{\omega_e}\right).$$

In Fig. 10 we display  $R = (Q/\pi) \ln \Delta$  against  $\tau_\sigma \omega_e$  for the three values,  $\alpha = 3/4$ ,  $3/8$ , and  $1/8$ . Note that there is no cusp in the graph for  $\alpha = 1/8$ , only a region of high curvature. Note also that by (4.11) the minimum value of  $Q$  for fixed  $\alpha$  is

$$Q_m = \frac{2\sqrt{\alpha}}{1 - \alpha},$$

so that for  $\alpha = 3/4$  we have  $Q_m = 4\sqrt{3} \approx 6.928$ . For this value of  $\alpha$  the maximum value of  $|R - 1|$  occurs at  $\omega_e = 0$ , where  $R = \sqrt{\alpha} \approx 0.866$ .

Finally, for the Achenbach-Chao model solid we obtain from (3.14) that

$$\frac{1}{Q} = \frac{2(1 - \alpha)\xi(\xi^2 + \alpha)}{(\xi^2 + \alpha)^2 - (1 - \alpha)^2 \xi^2}$$

with  $\xi = \tau_\sigma \omega_e$ . The asymptotic behavior for  $\xi \rightarrow 0$  is

$$\frac{1}{Q} = \frac{2(1 - \alpha)\xi}{\alpha} + O(|\xi|^3),$$

and

$$R = \alpha + O(\xi^2).$$

It is easy to see that the high-frequency behavior,  $\xi \rightarrow \infty$ , is given by

$$\frac{1}{Q} = \frac{2(1-\alpha)}{\xi} + O\left(\frac{1}{\xi^2}\right)$$

and

$$R = 1 + O\left(\frac{1}{\xi}\right).$$

It should be remembered, though, that for  $\alpha < 1/2$  it is impossible to obtain the proper high- and low-frequency behavior without introducing a branch cut. In Fig. 11 we display graphs of  $R$  as a function of  $\tau_0\omega_0$  for  $\alpha = 0.9, 0.7$ , and  $0.5$ . For  $\alpha = 0.5$  the curve has an angular bend arising from the right angle in Fig. 8.

We have found that for viscoelastic free vibrations the logarithmic decrement is asymptotic to  $1/(2Q)$  (i.e.,  $R \approx 1$ ) in the regimes in which the decay rate is small relative to the frequency of oscillation. This occurs for the Kelvin-Voigt solid at low frequencies, and the deviation at any particular frequency may be calculated from (4.9). We also have  $R \approx 1$  for the Maxwell solid at high frequencies, and the error may be obtained from (4.10). For the standard linear solid we have more choice as to the limits we wish to take. Thus, for  $\omega_0 \rightarrow \infty$  we have  $R \rightarrow 1$  uniformly in  $\alpha$ , for  $\omega_0 \rightarrow 0$  we have  $R/\sqrt{\alpha} \rightarrow 1$  uniformly in  $\alpha$ , and from Majda *et al.* (1985) we have that  $R \rightarrow 1$  uniformly in  $\omega_0$  as  $\alpha \rightarrow 1$ . For the Achenbach-Chao model solid we have the same three choices of parameter ranges:  $R \rightarrow 1$  uniformly in  $\alpha$  as  $\omega_0 \rightarrow \infty$ ,  $R/\alpha \rightarrow 1$  uniformly in  $\alpha$  as  $\omega_0 \rightarrow 0$ , and  $R \rightarrow 1$  uniformly in  $\omega_0$  as  $\alpha \rightarrow 1$ . For other values of the parameters, dispersion manifests itself in modifying the period of oscillation, giving rise in some circumstances to critical damping and to overdamping. Under these conditions the process-independent  $Q$  is not an adequate characterization of the dissipative process.

From our examples we conclude that the conjecture of O'Connell & Budiansky (1978) that dissipation may be measured by a process-independent  $Q$  is valid only when the dissipation rate is small relative to the frequency of oscillation, or alternatively, the requirement may be phrased as saying that the logarithmic decrement must be small. We have also given some idea of the range of validity of the conjecture for the viscoelastic models discussed here.

### Acknowledgment

The work of the first and second authors was performed under the auspices of the U. S. Department of Energy by the Lawrence Livermore National Laboratory under Contract No. W-7405-ENG-48.

### References

- Achenbach, J. D., 1975, *Wave Propagation in Elastic Solids*, North-Holland, Amsterdam.
- Achenbach, J. D., & Chao, C. C., 1962, A Three-Parameter Viscoelastic Model Particularly Suited for Dynamic Problems, *J. Mech. Phys. Solids*, **10**, 245–252.
- Bieberbach, L., 1953, *Conformal Mapping*, Chelsea, New York.
- Fisher, G. M. C., & Leitman, M. J., 1966, A Correspondence Principle for Free Vibrations of a Viscoelastic Solid, *ASME Trans. Ser. E J. Appl. Mech.*, **33**, 924–926.
- Gelfand, I. M., & Shilov, G. E., 1967, *Generalized Functions*, Vol. 3, *Theory of Differential Equations*, Academic Press, New York.
- Gurtin, M. E., & Herrera, I., 1965, On Dissipation Inequalities and Linear

- Viscoelasticity, *Quart. Appl. Math.*, **23**, 235–245.
- Kato, T., 1966, *Perturbation Theory for Linear Operators*, Springer-Verlag, New York.
- Leitman, M. J., & Fisher, G. M. C., 1973, The Linear Theory of Viscoelasticity, pp. 1–123 in *Handbuch der Physik*, Vol. VIa/3, ed. C. Truesdell, Springer-Verlag, Berlin-Heidelberg-New York.
- Majda, G., Chin, R. C. Y., & Followill, F. E., 1985, A Perturbation Theory for Love Waves in Anelastic Media, *Geophys. J. R. astr. Soc.*, **80**, 1–34.
- Naimark, M. A., 1968, *Linear Differential Operators*, Vol. 2, Ungar, New York.
- O'Connell, R. J., & Budiansky, B., 1978, Measures of Dissipation in Viscoelastic Media, *Geophys. Res. Lett.*, **5**, 5–8.
- Spencer, Jr., J. W., 1981, Stress Relaxations at Low Frequencies in Saturated Rocks: Attenuation and Modulus Dispersion, *J. Geophys. Res.*, **86**, 1803–1812.
- Thigpen, L., Hedstrom, G. W., & Bonner, B. P., 1983, Inversion of Creep Resoponse for Retardation Spectra and Dynamic Viscoelastic Functions, *ASME Trans. Ser. E J. Appl. Mech.*, **50**, 361–366.

### Appendix A Kelvin-Voigt solid

In this appendix we give the details of the analysis of (3.3), and we show why the two branches of Fig. 1 behave as they do. It is clear by inspection that  $p = -1$  and  $p = \infty$  are branch points of (3.3). We have to join these two branch points with a cut, and we shall see that the cut is to be taken from  $p = -1$  to  $p = \infty$  along the negative real axis. The question which is more interest to us, however, is the location of singularities in the  $\zeta$ -plane, because our task is the determination of the location of the image in the  $p$ -plane of the real axis in the  $\zeta$ -plane. To solve that problem, we may proceed in either of two ways: by analyzing (3.3) directly, or by looking for simpler intermediate transformations. We shall do it both ways, starting with a chain of intermediate transformations.

An inspection of (3.3) suggests the following sequence of transformations. With

$$p = z^2 - 1 \quad (\text{A.1})$$

Eq. (3.3) becomes the well-known Joukowski transformation (Bieberbach 1953)

$$\frac{1}{2} \left( z - \frac{1}{z} \right) = i\zeta \quad (\text{A.2})$$

This transformation is discussed in detail in Appendix E. The map (A.2) may be inverted,

$$z = i\zeta + \sqrt{1 - \zeta^2}. \quad (\text{A.3})$$

We see that there are branch points at  $\zeta = \pm 1$ . Note that the inverse function to (3.3) is a composition of (A.3) with (A.1) and that the mapping (A.1) preserves the singularities in (A.3) and adds no new ones. Thus, we need concern ourselves only with the branch points  $\zeta = \pm 1$ .

We have to use physical principles to determine the location of the cut and to specify the sheet for the mapping (A.3). For  $\zeta$  on the interval  $-1 < \zeta < 1$ , the form of (A.3) suggests the substitution  $\zeta = \sin \vartheta$ ,  $-\pi/2 \leq \vartheta \leq \pi/2$ . The two corresponding values of  $z$  and  $p$  are

$$z = e^{i\vartheta}, \quad p = e^{2i\vartheta} - 1, \quad (\text{A.4})$$

$$z = -e^{-i\vartheta}, \quad p = e^{-2i\vartheta} - 1. \quad (\text{A.5})$$

In both cases  $p$  goes around the circle of radius 1 with center at  $-1$ , as  $\vartheta$  goes from  $-\pi/2$  to  $\pi/2$ , but the direction is different. In order for (3.3) to be a perturbation of the elastic case  $p = i\zeta$  for values of  $\zeta \approx 0$ , we must choose the

counterclockwise branch (A.4). In Fig. 1 the curve (A.4) is shown as a solid circle and (A.5) as a dashed circle.

For  $\zeta$  on the real axis and  $\zeta > 1$ , the form of (A.3) suggests the substitution  $\zeta = \cosh \vartheta$ ,  $0 < \vartheta < \infty$ , which gives

$$z = ie^{\vartheta}, \quad p = -1 - e^{2\vartheta}, \quad (\text{A.6})$$

$$z = ie^{-\vartheta}, \quad p = -1 - e^{-2\vartheta}, \quad (\text{A.7})$$

For a Kelvin-Voigt solid the dynamic equation together with (3.1) is of parabolic type, so that  $\text{Re } p \rightarrow -\infty$  as  $\zeta \rightarrow \infty$  through real values. Consequently, we must choose the branch (A.6). This implies that as  $\zeta$  passes  $\zeta = 1$  in the increasing direction on the real axis, the image in the  $p$ -plane makes a  $90^\circ$  right turn. Consequently, the cut leaving the branch point  $\zeta = 1$  must lie in the upper halfplane. In fact, the entire cut from  $\zeta = -1$  to  $\zeta = 1$  must lie in the upper halfplane, for otherwise, the locus of the viscoelastic modes would have a discontinuity.

We still have to determine the image of the part of the real  $\zeta$  axis from  $\text{Re } \zeta = -\infty$  to  $\zeta = -1$ . An analysis similar to that given for (A.6) and (A.7) shows that if we set  $\zeta = -\cosh \vartheta$ ,  $0 < \vartheta < \infty$ , in (A.3), then the proper branch is

$$z = -ie^{\vartheta}, \quad p = -1 - e^{2\vartheta}. \quad (\text{A.8})$$

The complete proper image in the  $p$ -plane of the real axis in the  $\zeta$ -plane is shown as the solid curve in Fig. 1. The extraneous branch (A.7) is drawn with dashes. We conclude by noting that Fig. 1 shows that the cut in the  $p$ -plane for the square root in (3.3) is to be taken from  $p = -1$  to  $p = \infty$  along the negative real axis.

The other approach is to get as much information as possible directly from (3.3). We begin by differentiating (3.3),

$$\frac{d\zeta}{dp} = \frac{-i(p+2)}{4(p+1)^{3/2}}. \quad (\text{A.9})$$

The mapping (3.3) fails to be conformal at any point where  $d\zeta/dp$  is zero or does not exist. It is clear that these are the points  $p = -1$ ,  $p = -2$ , and  $p = \infty$ . Let us begin by examining (3.3) for  $p$  near  $-1$ . It is clear that  $p = -1$  maps onto  $\zeta = \infty$ , and it follows from (3.3) that the Laurent expansion for  $p$  about  $\zeta = \infty$  is of the form

$$p = -1 - \frac{1}{4\zeta^2} + O\left(\frac{1}{|\zeta|^4}\right) \quad (\text{A.10})$$

Consequently, for  $\zeta = Re^{i\vartheta}$  with  $R$  large,

$$p \approx -1 - \frac{e^{-2i\vartheta}}{4R^2},$$

so that an angle at  $p = -1$  is twice the size of the corresponding angle at  $\zeta = \infty$ . This is the reason for the U-turn at  $p = -1$  in the dashed curve in Fig. 1.

At  $p = -2$  it is clear from (A.9) that  $dp/d\zeta$  fails to exist, and the transformation inverse to (3.3) has singularities at the image points  $\zeta = \pm 1$ . In order to determine the type of singularity at, say,  $\zeta = 1$ , we make a Taylor expansion of (A.9) about  $p = -2$ , taking the branch for which  $\sqrt{p+1} = i$  at  $p = -2$ ,

$$\frac{d\zeta}{dp} = \frac{1}{4}(p+2) + O(|p+2|^2).$$

Integration of this approximation shows that



$$\zeta = 1 + \frac{1}{8}(p+2)^2 + O(|p+2|^3)$$

for  $p$  in a neighborhood of  $-2$ . Thus, for  $\zeta = 1 + re^{i\theta}$  with  $r$  small, we have

$$p = -2 + \sqrt{8r}e^{i\theta/2} + O(r).$$

This shows that an angle at  $\zeta = 1$  is mapped into an angle at  $p = -2$  of half the size, thus explaining the right angles at  $p = -2$  in Fig. 1. A similar analysis could be performed to show that there is another square-root singularity at  $\zeta = -1$ .

It remains to examine the case of  $p \rightarrow \infty$ . It follows directly from (3.3) that

$$p = -4\zeta^2 + O(1), \text{ as } \zeta \rightarrow \infty, \quad (\text{A.11})$$

and we see again that an angle at  $\zeta = \infty$  is doubled in size at  $p = \infty$ , this time on the other sheet.

We have seen that a simple analysis explains the sharp bends in the curves in Fig. 1, thus giving an understanding of the local behavior near critical points. To get the curves in Fig. 1 away from the critical points, we had to look at the global picture through the mappings (A.1) and (A.3). These ideas are important to our later discussion of the standard linear solid, because for it we can't construct a simple chain of transformations, and we use the computer to fill in the image curves between the critical points.

### Appendix B Maxwell Solid

In this section we analyze the mapping (3.7) to find out which values of  $p$  arise from real values of  $\zeta$ , thus determining the nature of the correspondence principle for a Maxwell solid.

We see immediately that there are branch points at  $p = 0$  and  $p = -1$ . Again, we may either analyze (3.7) directly or construct a sequence of simpler transformations. One such sequence is as follows. Let

$$\zeta = -2i\sqrt{w},$$

$$w = \xi^2 - \frac{1}{4},$$

and

$$\xi = p + \frac{1}{2}.$$

Since we are interested in the inverse function to (3.7), we invert these transformations and analyze

$$w = -\frac{\xi^2}{4}, \quad (\text{B.1})$$

$$\xi = \sqrt{w + \frac{1}{4}}, \quad (\text{B.2})$$

$$p = \xi - \frac{1}{2}. \quad (\text{B.3})$$

It is clear that the mapping (B.1) has no singularities. The mapping (B.2) has a branch point at  $w = -1/4$ , which is the image of the points  $\xi = \pm 1$ . The mapping (B.3) is just a translation and has no singularities. Thus, the only singularities for the inverse transformation to (3.7) are branch points of square-root type at  $\zeta = \pm 1$ .

Let us now determine the image of the real line in the  $\zeta$ -plane. It is clear that the transformation (B.1) maps the real axis of the  $\zeta$ -plane onto the negative real axis of the  $w$ -plane. For  $w$  real and  $-1/4 \leq w \leq 0$ , we see from (B.2) and (B.3) that  $\xi$  and  $p$  are real and that, depending on the branch of the square root, either

$$0 \leq \xi \leq \frac{1}{2}, \quad -\frac{1}{2} \leq p \leq 0, \quad (\text{B.4})$$

or

$$-\frac{1}{2} \leq \xi \leq 0, \quad -1 \leq p \leq -\frac{1}{2}. \quad (\text{B.5})$$

These are the two images of the real segment  $-1 \leq \zeta \leq 1$ . For  $w$  real with  $w < -1/4$ , we see that  $\xi$  is purely imaginary, with the two branches complex conjugate of each other. Consequently, the part of the real  $\zeta$  axis with  $|\zeta| \geq 1$  maps onto the line  $\text{Re } p = -1/2$ . The choice of the branch is determined as follows. Let us start with  $\zeta$  real and  $\zeta \approx \infty$ . Then in order for high-frequency modes in the Maxwell solid to behave like damped high-frequency elastic modes, we must have  $p \approx i\zeta$  as  $\zeta \rightarrow \infty$ . Thus, the segment  $-\infty < \zeta < -1$ ,  $\zeta$  real, is mapped onto the part of the line  $\text{Re } p = -1/2$  which lies in the third quadrant. Likewise, the segment  $1 < \zeta < \infty$ ,  $\zeta$  real, is mapped onto the part of the line  $\text{Re } p = -1/2$  which lies in the second quadrant. Since there must be no damping in the zero-frequency limit, the branch (B.5) is extraneous, and we must choose the branch (B.4). The full image is shown in Fig. 2. Just as for the Kelvin-Voigt solid, we see by the angles at the corners that the cut from  $\zeta = -1$  to  $\zeta = 1$  must lie in the upper half of the  $\zeta$ -plane.

As we did for the Kelvin-Voigt solid, we can get a great deal of qualitative information about the inverse to (3.7) by analyzing the behavior of (3.7) near critical points. We begin by differentiating (3.7) to get

$$\frac{d\zeta}{dp} = \frac{-i(2p+1)}{\sqrt{p(p+1)}}.$$

Thus, we see that  $d\zeta/dp = 0$  at  $p = -1/2$ , and  $d\zeta/dp = \infty$  at  $p = 0$  or  $p = -1$ . The mapping (3.7) is regular at  $p = \infty$ . Let us examine first the behavior near  $p = -1/2$ , which by (3.7) corresponds to  $\zeta = \pm 1$ . Just as for the Kelvin-Voigt solid, we expand  $d\zeta/dp$  in a Taylor series about the critical point,

$$\frac{d\zeta}{dp} = -4\left(p + \frac{1}{2}\right) + O(|p + \frac{1}{2}|^2). \quad (\text{B.6})$$

Upon integrating (B.6), we see that for  $p = -1/2 + re^{i\theta}$ , we have

$$\zeta \pm 1 = -2r^2 e^{2i\theta} + O(r^3),$$

so that angles at the branch points  $\zeta = \pm 1$  are mapped into angles of half the size at  $p = -1/2$ . Similarly, expansions of (3.7) about  $p = 0$  and  $p = -1$  show that an angle at  $\zeta = 0$  is mapped into an angle twice the size at  $p = 0$  or at  $p = -1$ .

### Appendix C Standard Linear Solid

In Figs. 3–6 for four values of  $\alpha$  we show the three images in the  $p$ -plane of the real axis in the  $\zeta$ -plane under the transformation (3.11). The principal branch is shown as a solid curve, a choice dictated by the fact that for low frequencies ( $\zeta \approx 0$ ), a standard linear solid behaves like a Kelvin-Voigt solid, and for high frequencies ( $\zeta \approx \infty$ ), it behaves like a Maxwell solid. This appendix is devoted to an explanation of these figures based on local information.

Let us begin with an analysis of the low-frequency behavior, with a verification of (3.12). For the physical branch of the square root in (3.11),

application of the binomial expansion shows that the Maclaurin series of  $\zeta$  as a function of  $p$  is of the form

$$\zeta = \frac{-ip}{\sqrt{a}} \left[ 1 - \frac{(1-a)p}{2a} \right] + O(|p|^3)$$

as  $p \rightarrow 0$ . Thus, the inverse function has a Maclaurin series of the form

$$p = i\zeta\sqrt{a} - \frac{1-a}{2}\zeta^2 + O(|\zeta|^3) \quad (\text{C.1})$$

as  $\zeta \rightarrow 0$ . We now obtain (3.12) upon transforming to physical variables. Note that if we take the other branch of the square root in (3.11), the coefficients in (C.1) are replaced by their complex conjugates. Thus, two branches in Figs. 3–6 lie on top of each other but have the opposite orientation.

It is clear that (3.11) has branch points at  $p = -1$  and  $p = -a$ . (Note that  $0 < a < 1$  by assumption.) We take the branch cut to be the interval from  $p = -1$  to  $p = -a$ , ensuring that the curves in Figs. 3–6 never cross the cut.

Let us now examine the high-frequency behavior. It follows directly from (3.11) that  $p = \infty$  is a regular point. In fact, we find that as  $\zeta \rightarrow \infty$  one branch of the inverse to (3.11) has Laurent expansion of the form

$$p = i\zeta - \frac{1-a}{2} + O\left(\frac{1}{|\zeta|}\right). \quad (\text{C.2})$$

This explains the vertical asymptotes in Figs. 3–6. Eq. (3.13) is just (C.2) rewritten in terms of the physical variables.

Let us now find the points at which the mapping (3.11) is not conformal. Upon differentiating (3.11), we find that

$$\frac{d\zeta}{dp} = \frac{-i(2p^2 + (3a+1)p + 2a)}{(p+1)^{1/2}(p+a)^{3/2}}. \quad (\text{C.3})$$

It is clear that  $d\zeta/dp = 0$  at the zeros  $p_1$  and  $p_2$  of  $2p^2 + (3a+1)p + 2a$  and that  $d\zeta/dp = \infty$  at the points  $p = -a$  and  $p = -1$ . An expansion of (3.11) about  $p = -1$  shows that angles at  $\zeta = 0$  are doubled at  $p = -1$ . Similarly, an expansion of (3.11) about  $p = -a$  shows that on this branch angles at  $\zeta = \infty$  are doubled at  $p = -a$ .

Each of the points

$$p_1 = -\frac{(3a+1)}{4} + \frac{1}{4}\sqrt{(1-a)(1-9a)}, \quad (\text{C.4})$$

$$p_2 = -\frac{(3a+1)}{4} - \frac{1}{4}\sqrt{(1-a)(1-9a)}, \quad (\text{C.5})$$

is the image of two branch points in the  $\zeta$ -plane. The reason for the multiplicity is that in (3.11) there are two values of  $\zeta$  for every nonzero finite value of  $p$ . In Figs. 3–6 the values of  $p_1$  and  $p_2$  are marked with x's.

We consider three cases, depending on whether the  $p_j$  are real and distinct, equal (and real), or complex. We begin with  $a = 1/9$  because we want the sheet structure in the  $\zeta$ -plane to depend continuously on  $a$ . For  $a = 1/9$  the numerator of (C.3) has a zero of second order at  $p = p_1 = p_2$ . That is, the Taylor series for  $d\zeta/dp$  about  $p = p_1$  is of the form

$$\frac{d\zeta}{dp} = \frac{-2i(p - p_1)^2}{(p_1 + 1)^{1/2}(p_1 + a)^{3/2}} + O(|p - p_1|^3).$$

Consequently, the Taylor series for  $\zeta(p)$  about  $p = p_1$  has the form

$$\zeta = c_0 + c_3(p - p_1)^3 + O(|p - p_1|^4)$$

with  $c_3 \neq 0$ . In fact, it is easy to see from (3.11) that  $c_0 = \pm 1/\sqrt{3}$ . Thus, for the inverse function with  $\alpha = 1/9$  each of the branch points  $\zeta = \pm 1/\sqrt{3}$  is a cube-root singularity. In order to have consistency with a Kelvin-Voigt solid at low frequencies and a Maxwell solid at high frequencies, we see that the cut from  $\zeta = -1/\sqrt{3}$  to  $\zeta = 1/\sqrt{3}$  must lie above the real axis. The structure of the three sheets in the  $\zeta$ -plane is shown in Fig. 12 in a cross section taken along the imaginary axis.

For  $\alpha = 1/9$  the three images in the  $p$ -plane of the real axis in the  $\zeta$ -plane may be explained as follows (see Fig. 4). As  $\text{Re } \zeta$  starts from  $-\infty$ , the principal branch starts up the solid path (C.2) in the third quadrant. One extraneous branch is the complex conjugate of this one, and it corresponds to the dashed line on sheet 3 in Fig. 12. (If we start on sheet 1 and go around the branch point in the clockwise direction, we cross the cut from above, winding up on sheet 3. The corresponding angle swept out in the  $p$ -plane is  $-120^\circ$ .) The other extraneous branch starts at  $p = -\alpha$ , and it is the image of the dashed line on sheet 2 in Fig. 12. As  $\zeta$  passes the branch point  $\zeta = -1/\sqrt{3}$ , for each of the branches  $p$  executes a  $60^\circ$  right turn (because of the cube root). For the principal branch the path goes around the loop in the counterclockwise direction. At  $\zeta = 0$  the three images are  $p = 0, 0, -1$ . At the branch point  $\zeta = 1/\sqrt{3}$  the paths make another  $60^\circ$  turn to the right. The principal path connects with (C.2) as  $\zeta \rightarrow \infty$ . In order to draw Fig. 4, we used this local analysis to determine the behavior at  $p = \infty, 0, p_1, -\alpha$ , and  $-1$ , and we used Newton's method and continuation in  $\zeta$  to find how the local pieces join together.

Let us now examine the complex case:  $1/9 < \alpha < 1$ . In that case the values of  $p_1$  and  $p_2$  in (C.4) and (C.5) are complex conjugates of each other, and it follows from (3.11) that the corresponding branch points in the  $\zeta$ -plane are located at the vertices of a rectangle with center at the origin and sides parallel to the real and imaginary axes. See Fig. 13. The main step involves showing that

$$\frac{p_1 + 1}{p_1 + \alpha} = \frac{-w}{w^*} = -e^{2i\vartheta},$$

where

$$w = \sqrt{(1-\alpha)} + i\sqrt{(9\alpha-1)} = re^{i\vartheta},$$

and  $w^*$  denotes the complex conjugate of  $w$ . Similarly, we have

$$\frac{p_2 + 1}{p_2 + \alpha} = \frac{-w^*}{w} = -e^{-2i\vartheta}.$$

Thus, with  $p = \rho e^{i\varphi}$  in (C.4), the four branch points are  $\zeta = \pm \rho e^{\pm i(\varphi + \vartheta)}$ . This analysis shows that for  $1/9 < \alpha < 1$  the real axis in the  $\zeta$ -plane does not hit the branch points. Consequently, the only local analysis we have to take into account is that involving  $\zeta \rightarrow 0$  and  $\zeta \rightarrow \infty$ , and this is the same as for  $\alpha = 1/9$ . In Figs. 5 and 6 we use Newton's method and continuation in  $\zeta$  to join these local pieces to form the global images of the real axis in the  $\zeta$ -plane.

Note that between Figs. 4 and 5 the principal branch varies continuously with  $\alpha$ , while the other branches are discontinuous. This may be accomplished with a continuous sheet structure if the cuts for  $1/9 < \alpha < 1$  are taken as in Fig. 13 with the cross section of the sheets on the imaginary axis as shown in Fig. 14. In Figs. 12 and 14 the principal branch of the real axis is marked with a solid line.

It remains to consider  $0 < \alpha < 1/9$ , and we see from (C.4) and (C.5) that  $p_1$  and  $p_2$  are real and that  $-1 < p_2 < p_1 < -\alpha$ . Consequently, by (3.11) the corresponding values  $\zeta_1$  and  $\zeta_2$  are also real, and the two values of  $\zeta$  for each  $p_j$

are negatives of each other. We join each of these pairs of branch points with a cut just above the real axis. It is easy to see that each of these branch points is of square-root type, explaining the  $90^\circ$  turns in Fig. 3. Finally, in order for the sheet structure to be continuous as  $a \rightarrow 1/9$  and consistent with Fig. 3, we see that for  $|\operatorname{Re} \zeta| < \zeta_1$  the sheets are as in Fig. 12, and for  $\zeta_1 < |\operatorname{Re} \zeta| < \zeta_2$  sheets 1 and 3 cross just above the real axis, while sheet 2 is undisturbed.

From an inspection of Figs. 4–6 we might expect that  $\Gamma$  lies in a strip in the  $p$ -plane. This is indeed the case. A precise statement of this result is given in the following theorem.

**THEOREM 1.** *The viscoelastic free vibrations of a standard linear solid with  $0 < a < 1$  lie in the strip*

$$\{ p \mid -\frac{1-a}{2} < \operatorname{Re} p \leq 0 \},$$

and for  $p \neq 0$  they are always dissipative, i. e.,  $\operatorname{Re} p < 0$ .

**Remarks.** The dissipative nature of the viscoelastic modes is to be expected from the dissipativity principle of Gurtin & Herrera (1965). Note also that the edges of the strip are just what is prescribed by the behavior (C.2) as  $\zeta \rightarrow \infty$  and by the fact that  $p = 0$  at  $\zeta = 0$ .

**Proof.** We show by elementary arguments that if  $p = x + iy$  with  $y \neq 0$  such that (3.11) is satisfied for real  $\zeta$ , then  $-(1-a)/2 < x < 0$ . This is equivalent to Theorem 1. We begin by transforming the problem to a question of determining the location of the real zeros of a cubic polynomial in  $x$  with coefficients depending on  $a$  and  $y$ .

If we square both sides of (3.11) and multiply by  $-(p+a)(p^*+a)$ , we obtain the relation

$$p^2(p+1)(p^*+a) = -|p+a|^2\zeta^2, \quad (\text{C.6})$$

where  $p^* = x - iy$ . For  $\zeta$  real the right-hand side of (C.6) is real. Thus, upon setting the imaginary part of the left-hand side of (C.6) equal to zero with  $p = x + iy$ , we find that

$$(2x^3 + (1+3a)x^2 + 2(a+y^2)x + (1-a)y^2)y = 0. \quad (\text{C.7})$$

Note that the right-hand side of (C.6) is real when  $\zeta$  is pure imaginary, so that (C.7) also contains the images of the imaginary axis in the  $\zeta$ -plane. In particular, this includes the part of the real axis  $y = 0$  with  $x > -a$  or  $x < -1$ , as is easily seen from (3.11). In any case, the trivial solution  $y = 0$  is not of interest to us. Therefore, we are led to the question of locating the zeros of the polynomial in  $x$ ,

$$f(x) = 2x^3 + (1+3a)x^2 + 2(a+y^2)x + (1-a)y^2. \quad (\text{C.8})$$

Since  $0 < a < 1$ , it is clear from (C.8) that  $f(x) > 0$  if  $x \geq 0$  and  $y \neq 0$ . Thus, we have shown that the solutions of (3.11) for real  $\zeta$  lie in the halfplane  $\operatorname{Re} p \leq 0$  with only the point  $p = 0$  lying on the boundary.

In order to show that  $\operatorname{Re} p$  is bounded from below by  $-(1-a)/2$  for  $p$  on  $\Gamma$ , let us begin by performing a combined shift and reflection in (C.8). Upon setting  $x = -z - (1-a)/2$  and

$$g(z) = -f\left(-z - \frac{1-a}{2}\right),$$

we find that

$$g(z) = 2z\left(z - \frac{3a-1}{2}\right)^2 + 2y^4z + a^2(1-a).$$

Thus, it is clear that  $g(z) > 0$  if  $z \geq 0$  and  $0 < a < 1$ . In other words, we have shown

that  $f(x) < 0$  if  $x \leq -(1-\alpha)/2$ . That is, the zeros of  $f(x)$  are restricted to lie in the interval  $-(1-\alpha)/2 < x \leq 0$ , and the curve  $\Gamma$  lies in the strip  $-(1-\alpha)/2 < \text{Re } p \leq 0$ . This completes the proof of the theorem.

#### Appendix D Achenbach-Chao Model Solid

In this appendix we analyze (3.15) and explain Figs. 6–9. In order to understand the mapping (3.15) from a global point of view, we write it as a sequence of simpler mappings. In fact, (3.15) is equivalent to the sequence:

$$z = \frac{p + \alpha}{\sqrt{\alpha(1-\alpha)}}, \quad (\text{D.1})$$

$$\xi = \frac{1}{2}\left(z - \frac{1}{z}\right), \quad (\text{D.2})$$

and

$$\zeta = -i(\sqrt{\alpha(1-\alpha)}\xi - \alpha + \frac{1}{2}). \quad (\text{D.3})$$

Eq. (D.1) consists of a translation and a change of scale. Eq. (D.3) performs a scale change, a translation, and a rotation. Eq. (D.2) is the well-known Joukowski transformation. It appears in the discussion of the Kelvin-Voigt solid and is discussed in Appendix E. Thus, the essential feature of (3.15) is the Joukowski transformation, describing ideal flow past a circular cylinder. The break in the physical branch for  $\alpha = 0.3$  illustrates the situation for  $\alpha < 0.5$ , and it may be explained as follows. The inverse mapping to (D.2) is

$$z = \xi + \sqrt{\xi^2 + 1},$$

which has branch points at  $\xi = \pm i$ . Consequently, by (D.3) the branch points in the  $\zeta$ -plane are located at

$$\zeta = \pm \sqrt{\alpha(1-\alpha)} + \left(\alpha - \frac{1}{2}\right)i. \quad (\text{D.4})$$

Thus, we see that the branch points cross the real axis of the  $\zeta$ -plane at  $\alpha = 1/2$ , which causes the behavior for  $\alpha < 1/2$  to be different from that for  $\alpha > 1/2$ .

In order to understand this phenomenon, let us perform a local analysis, starting with an examination of the high-frequency ( $\zeta \rightarrow \infty$ ) and low-frequency ( $\zeta \rightarrow 0$ ) limits. It is clear from (3.15) that the two images of  $\zeta = \infty$  are  $p = \infty$  and  $p = -\alpha$ . In fact, a slightly more detailed analysis of (3.15) shows that as  $\zeta \rightarrow \infty$  these two branches have Laurent expansions of the form

$$p = 2i\zeta - (1-\alpha) + O\left(\frac{1}{|\zeta|}\right) \quad (\text{D.5})$$

and

$$p = -\alpha + \frac{i\alpha(1-\alpha)}{2\zeta} + O\left(\frac{1}{|\zeta|^2}\right). \quad (\text{D.6})$$

It is clear that the branch (D.5) is a perturbation of the elastic case  $p = 2i\zeta$ , while (D.6) is not.

From (3.15) it is evident that the images of  $\zeta = 0$  are  $p = 0$  and  $p = -1$ , but only the branch  $p = 0$  makes sense physically. Thus, it would seem as if all we have to do is to extend the branch (D.5) until it goes through  $p = 0$  at  $\zeta = 0$ . This turns out to be possible only if  $\alpha \geq 1/2$ .

It is true that we have already found in (D.4) the locations of the branch points, but alternatively, we could also do this by a local analysis. Upon differentiating (3.15), we see that

$$\frac{d\zeta}{dp} = \frac{p^2 + 2\alpha p + \alpha}{2i(p + \alpha)^2},$$

so that  $d\zeta/dp = 0$  and  $dp/d\zeta$  fails to exist when  $p$  takes on the values

$$p_1 = -\alpha + i\sqrt{\alpha(1-\alpha)},$$

$$p_2 = -\alpha - i\sqrt{\alpha(1-\alpha)}.$$

The images of these points are the points (D.4),

$$\zeta_1 = \sqrt{\alpha(1-\alpha)} + (\alpha - \frac{1}{2})i \quad (D.7)$$

and

$$\zeta_2 = -\sqrt{\alpha(1-\alpha)} + (\alpha - \frac{1}{2})i, \quad (D.8)$$

and it is easy to show that they are branch points of square-root type. We see from (D.7) and (D.8) that  $\zeta_1$  and  $\zeta_2$  lie on the circle

$$\gamma = \{\zeta: |\zeta| = 1/2\}$$

and that they lie in the upper half of the  $\zeta$ -plane if  $1/2 < \alpha < 1$  and in the lower half if  $0 < \alpha < 1/2$ . This implies that for  $\alpha > 1/2$  if we connect the branch points by a cut in the upper half plane and if the location of the cut depends continuously on  $\alpha$ , then in every neighborhood of  $\alpha = 1/2$  the image in the  $p$ -plane of the real axis in the  $\zeta$ -plane must have some sort of discontinuity. Either the cut lies completely in the lower half plane for  $\alpha < 1/2$  resulting in violation of the (D.5) as  $\zeta \rightarrow \infty$  or of  $p = 0$  at  $\zeta = 0$ , or the cut crosses the real  $\zeta$  axis, resulting in breaks in the image curve but maintaining (D.5) as  $\zeta \rightarrow \infty$  and  $p = 0$  at  $\zeta = 0$ . In Fig. 7 for  $\alpha = 0.3$  we have chosen the second option, arbitrarily taking the cut to be the lines  $\text{Re } \zeta = \pm \sqrt{\alpha(1-\alpha)}$ ,  $\text{Im } \zeta \geq \alpha - 1/2$ . This behavior implies that for  $\alpha < 1/2$  it is not possible to represent the solution of a dynamic viscoelastic wave problem in terms of modes alone; the contribution of contour integrals around the branch points must also be included.

### Appendix E The Joukowski Transformation

For the sake of completeness we include here a brief discussion of the Joukowski transformation

$$w = \frac{1}{2}(z - \frac{1}{z}), \quad (E.1)$$

which we met in our discussion of the Achenbach-Chao model solid in Eq. (D.2) and of the Kelvin-Voigt solid in Eq. (A.2). (Actually, Eq. (A.2) contains an additional factor  $-i$  which merely performs a rotation by  $-90^\circ$ .) Similar analysis of the Joukowski transformation may be found in classical references on conformal mapping, such as the book by Bieberbach (1953).

We begin by examining the images in the  $w$ -plane of circles  $z = re^{i\vartheta}$  in the  $z$ -plane parameterized by the radius  $r$ . We see from a direct substitution that

$$\text{Re } w = \frac{1}{2}(\tau - \frac{1}{\tau})\cos \vartheta, \quad \text{Im } w = \frac{1}{2}(\tau + \frac{1}{\tau})\sin \vartheta. \quad (E.2)$$

Thus, the unit circle  $z = e^{i\vartheta}$  is collapsed onto the segment from  $w = -i$  to  $w = i$ . In our analysis of the Kelvin-Voigt and Achenbach-Chao solids we actually used the mapping inverse to (E.1). It is for this reason that a circle appears as the image of a line segment in Figs. 1 and 8.

For values of  $r$  different from 1 we see from (E.2) that the image in the  $w$ -plane is an ellipse centered on the origin with major axis of length  $(\tau + 1/\tau)/2$

and on the imaginary axis and with minor axis of length  $(\tau - 1/\tau)/2$ . Thus, each of these ellipses has its foci at  $w = \pm i$ , and the segment we obtained when  $\tau = 1$  is merely a degenerate ellipse of this family. Note that for  $\tau > 1$  the circles in the  $z$ -plane of radius  $\tau$  and  $1/\tau$  map onto the same ellipse in the  $w$ -plane.

In our discussion of the Achenbach-Chao model solid we were interested not in the inverse images of ellipses, but of lines,  $\text{Re } w = \text{constant}$ . The images in the  $z$ -plane of several such lines are shown in Fig. 15. They represent the streamlines of irrotational flow past a circular cylinder, and that is the reason for the classical interest in the mapping. Note in Fig. 15 the special role played by the circle  $|z| = 1$ , separating the external flow field from the internal flow field. We have seen that the inverse transformation to (E.1) is double valued. This is shown in Fig. 15 by the fact that each line,  $\text{Re } w = \text{constant} \neq 0$ , is mapped onto an exterior streamline and an interior streamline. In Fig. 15 one of these images is drawn as a solid curve and the other with dashes. We have chosen rather unusual cuts ( $\text{Im } w = \pm 1, \text{Re } w \leq 0$ ) in keeping with the cuts introduced in Appendix D. Thus, the curves shown in Figs. 7-9 are simply individual curves from Fig. 15 with appropriate translation and scaling.



**List of Figures.**

1. Kelvin-Voigt solid.
2. Maxwell solid.
3. Standard linear solid,  $\alpha = 0.08$ .
4. Standard linear solid,  $\alpha = 0.111$ .
5. Standard linear solid,  $\alpha = 0.125$ .
6. Standard linear solid,  $\alpha = 0.75$ .
7. Achenbach-Chao solid,  $\alpha = 0.3$ .
8. Achenbach-Chao solid,  $\alpha = 0.5$ .
9. Achenbach-Chao solid,  $\alpha = 0.7$ .
10.  $R$  for the standard linear solid.
11.  $R$  for the Achenbach-Chao solid.
12. Cross section of the sheets,  $\alpha = 1/9$ .
13. Location of the cuts,  $1/9 < \alpha < 1$ .
14. Cross section of the sheets,  $1/9 < \alpha < 1$ .
15. Joukowski streamlines.

## Kelvin–Voigt Solid

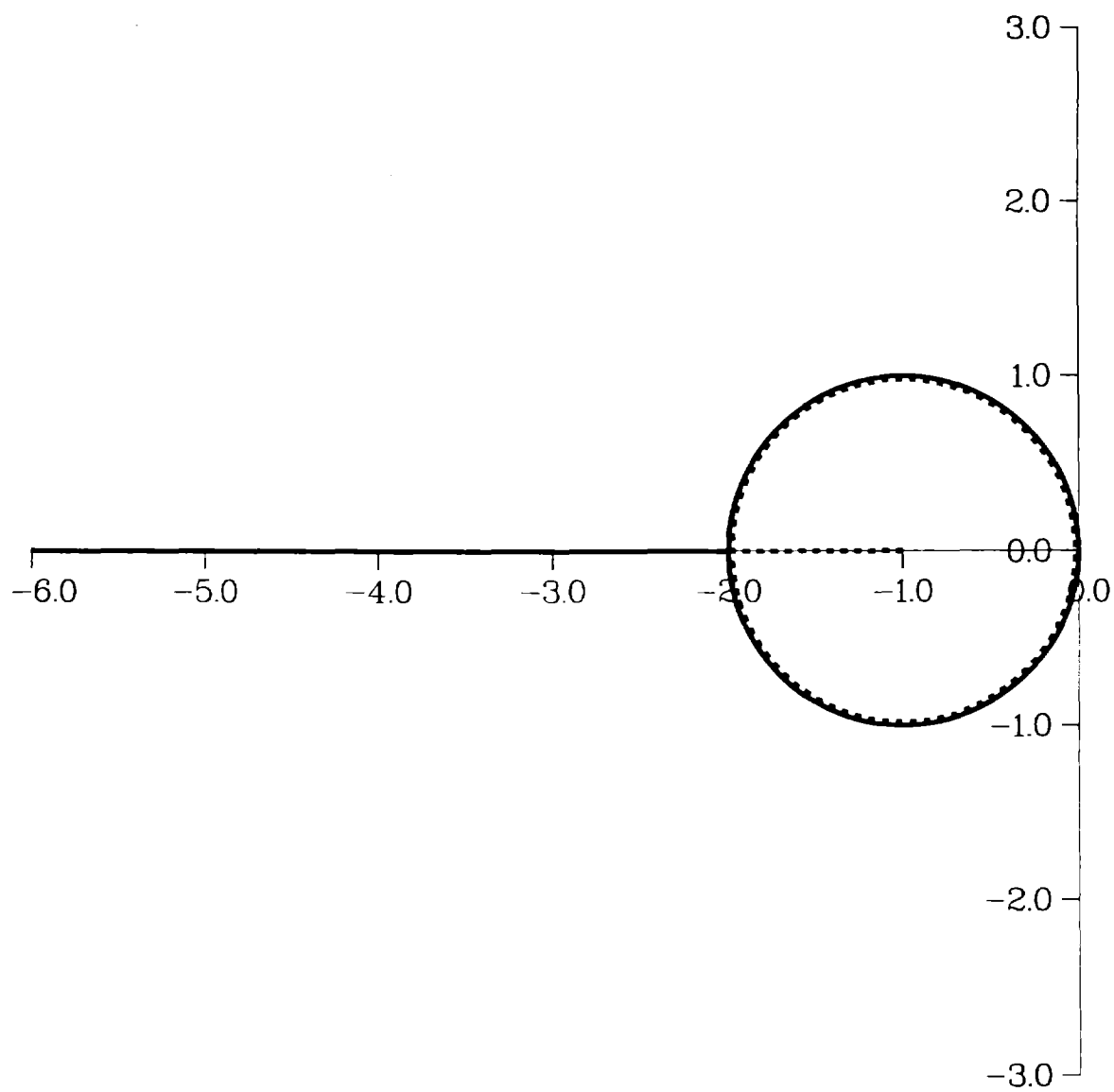


Fig. 1

# Maxwell Solid

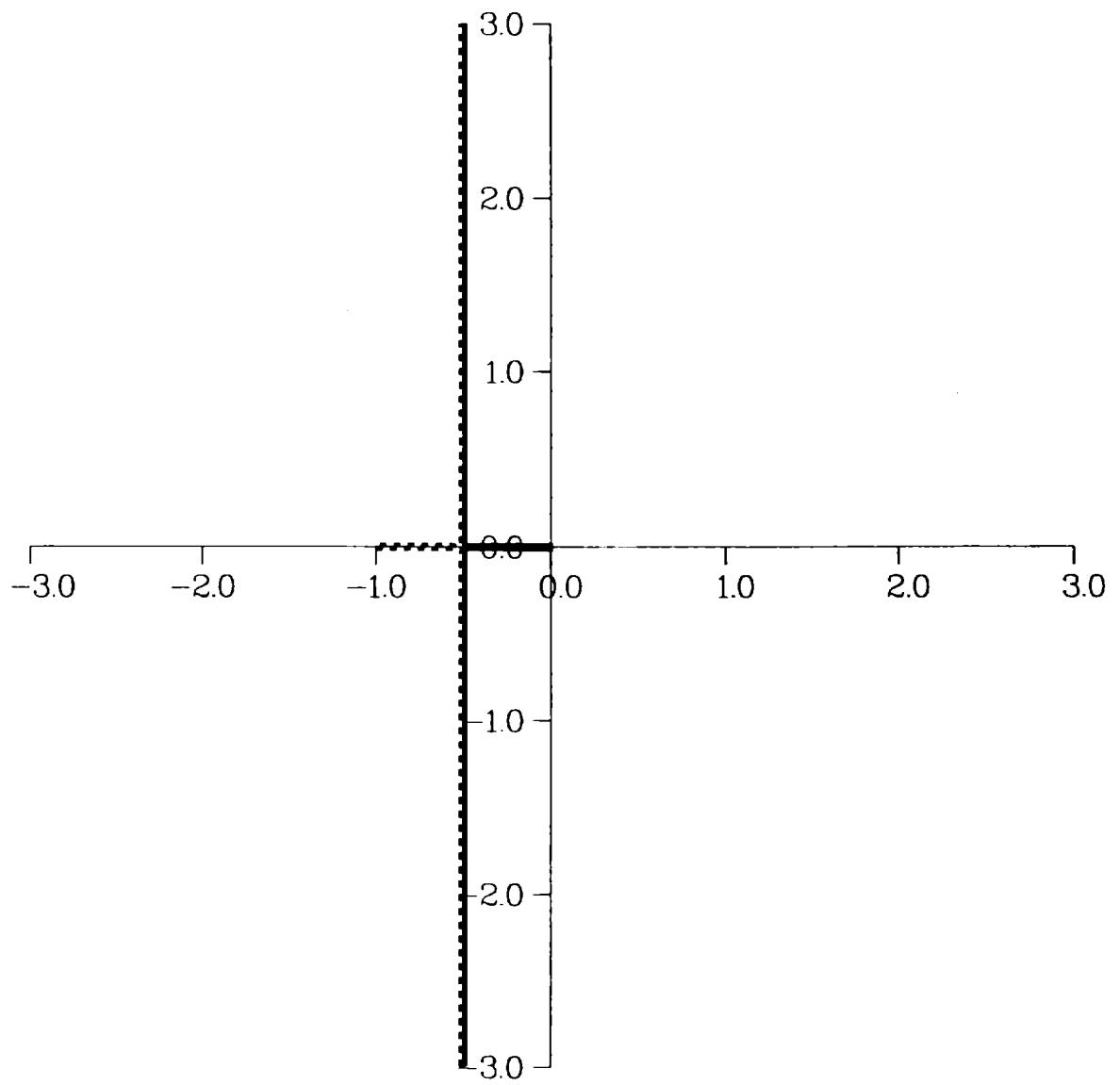
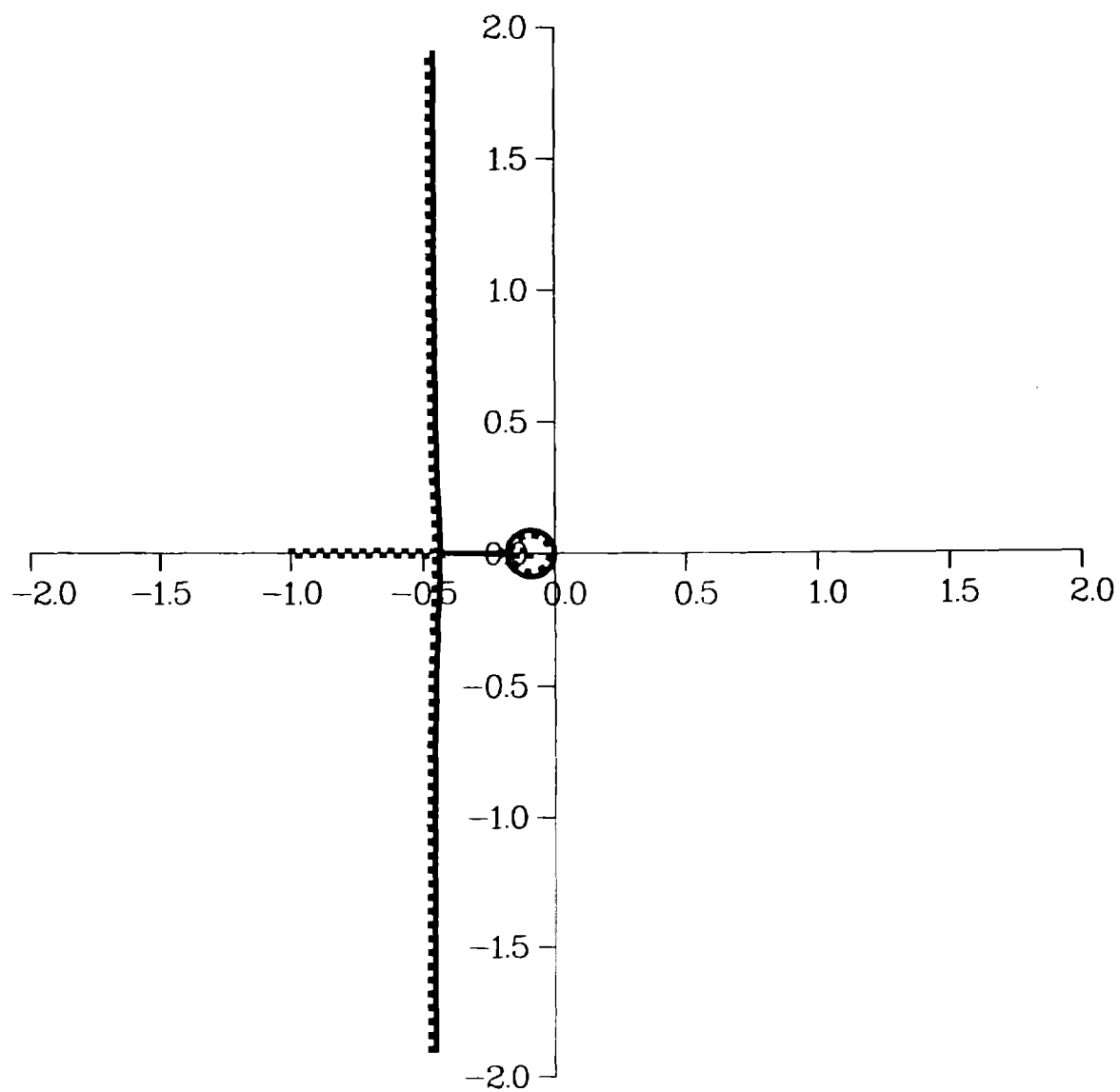


Fig. 2

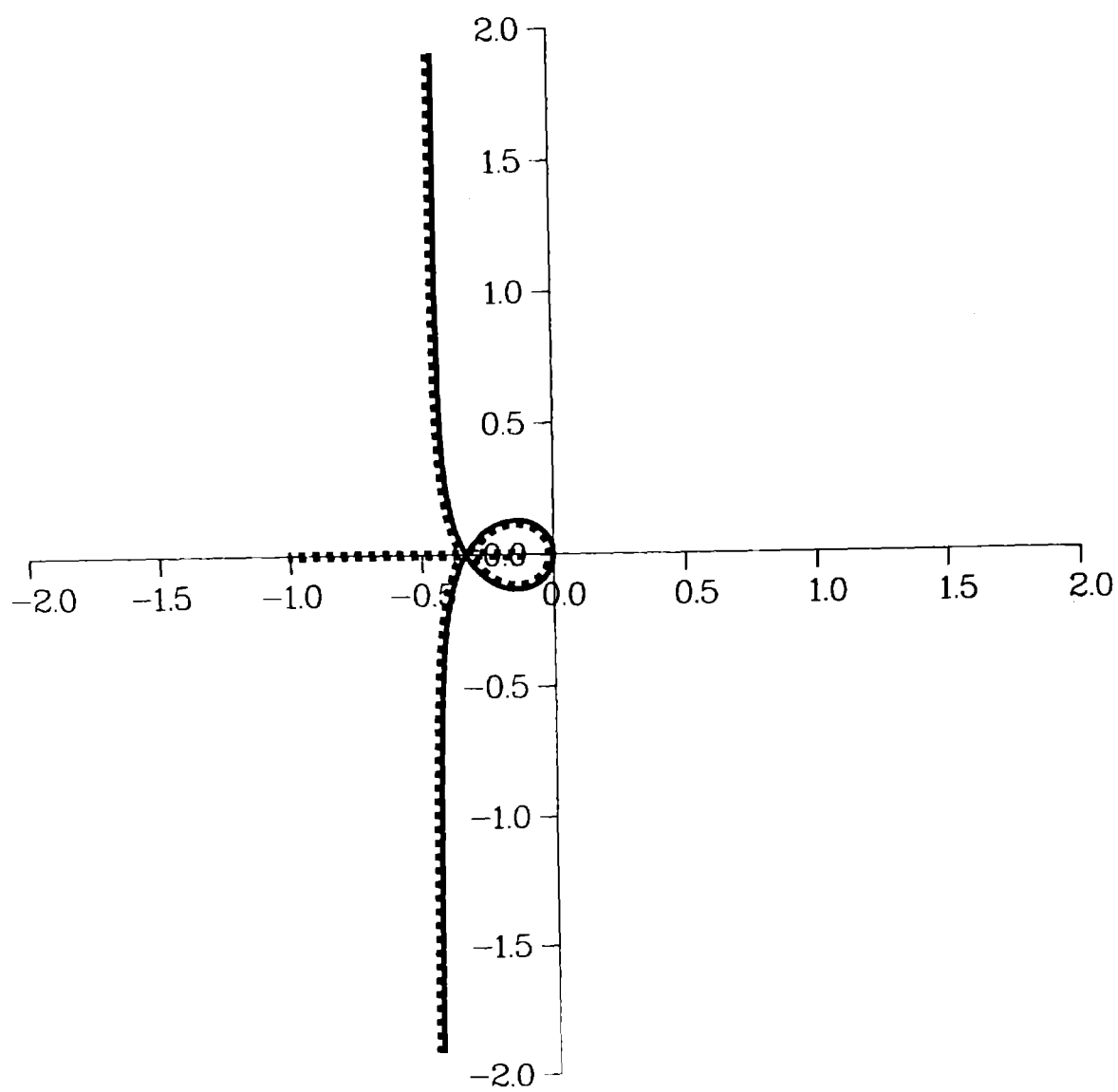
## Standard Linear Solid



$$a = 0.080$$

Fig. 3

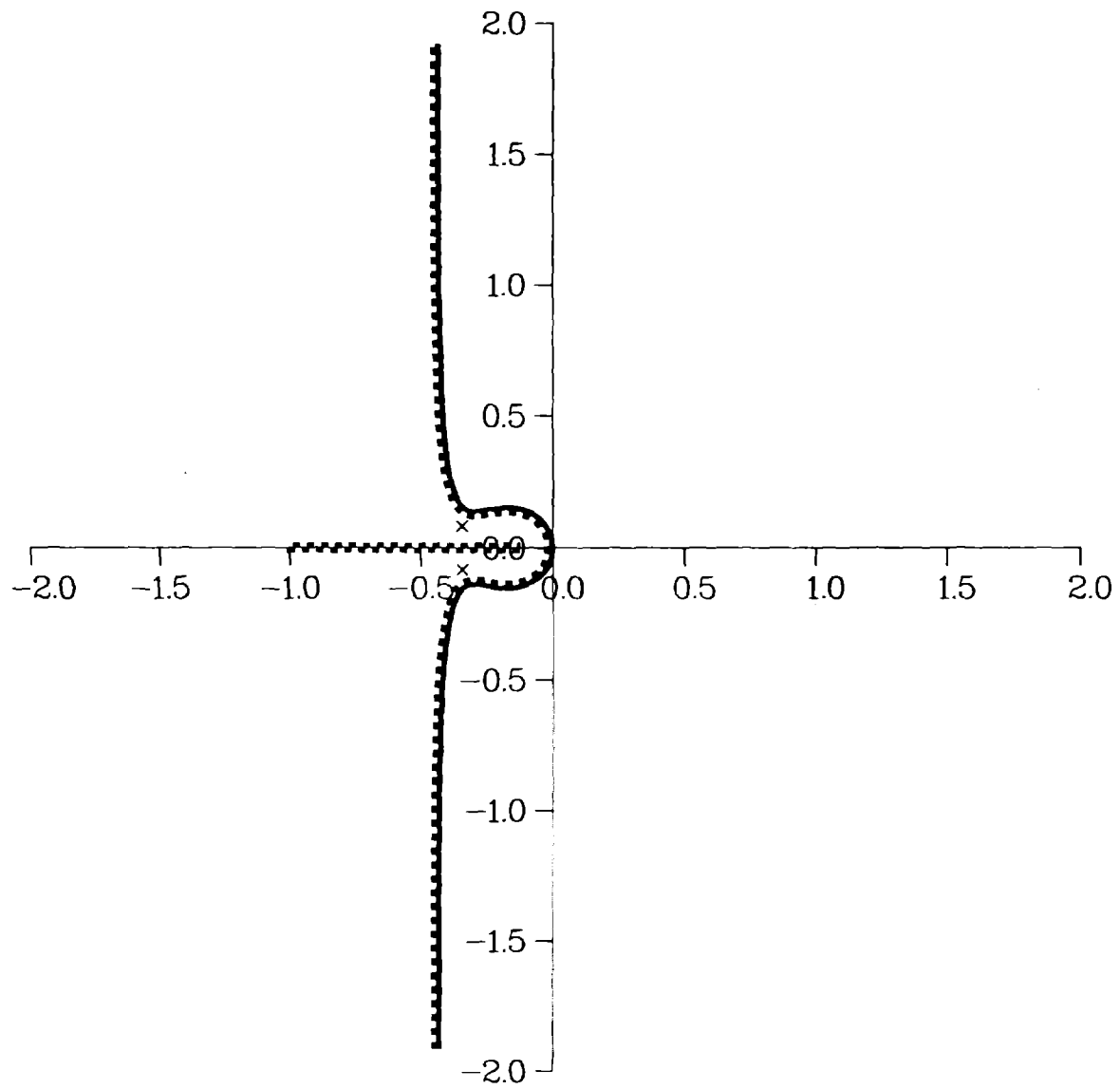
## Standard Linear Solid



$$a = 0.111$$

Fig. 4

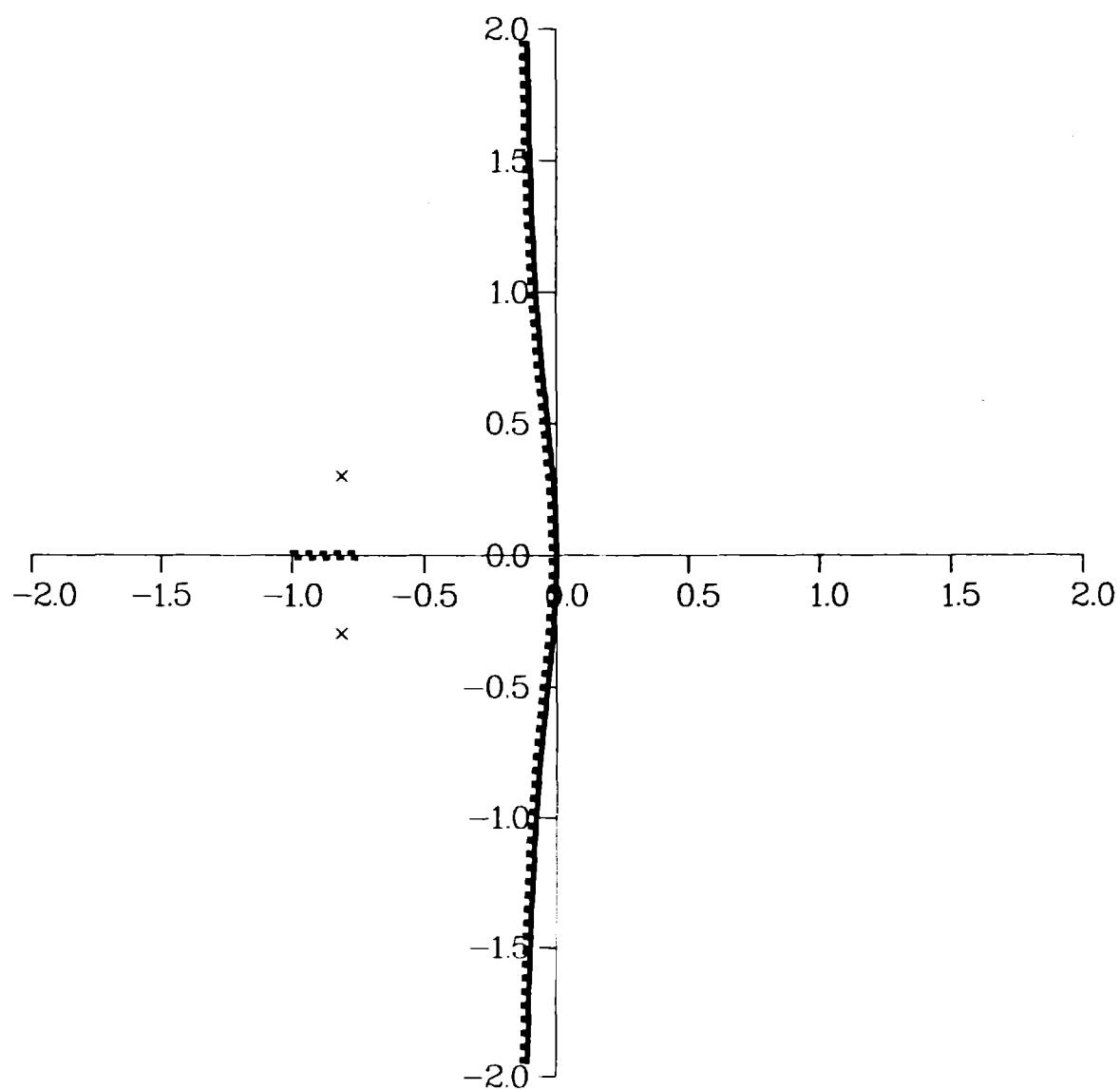
## Standard Linear Solid



$$a = 0.125$$

Fig. 5

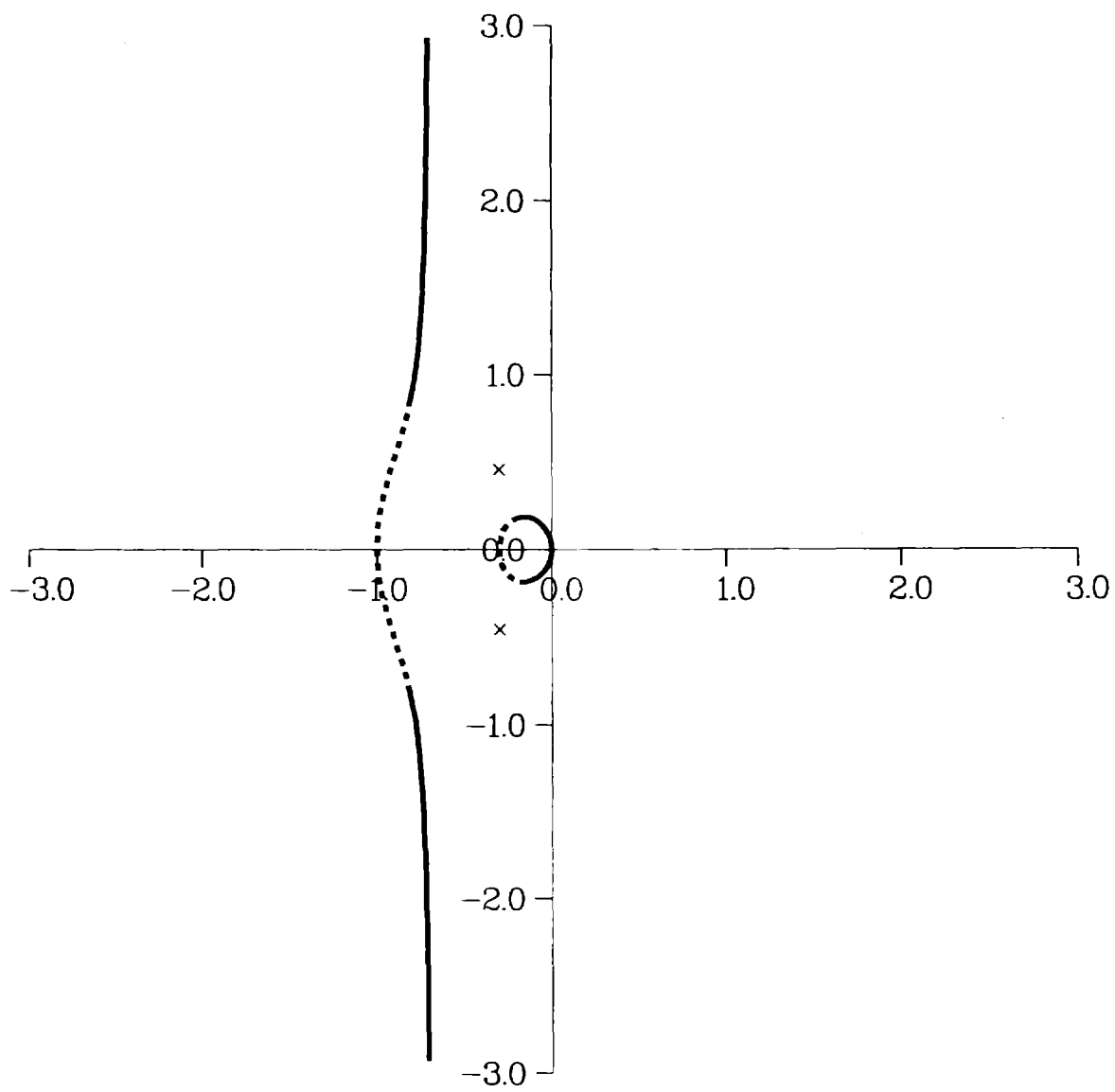
# Standard Linear Solid



$$a = 0.750$$

Fig. 6

# Achenbach–Chao Solid

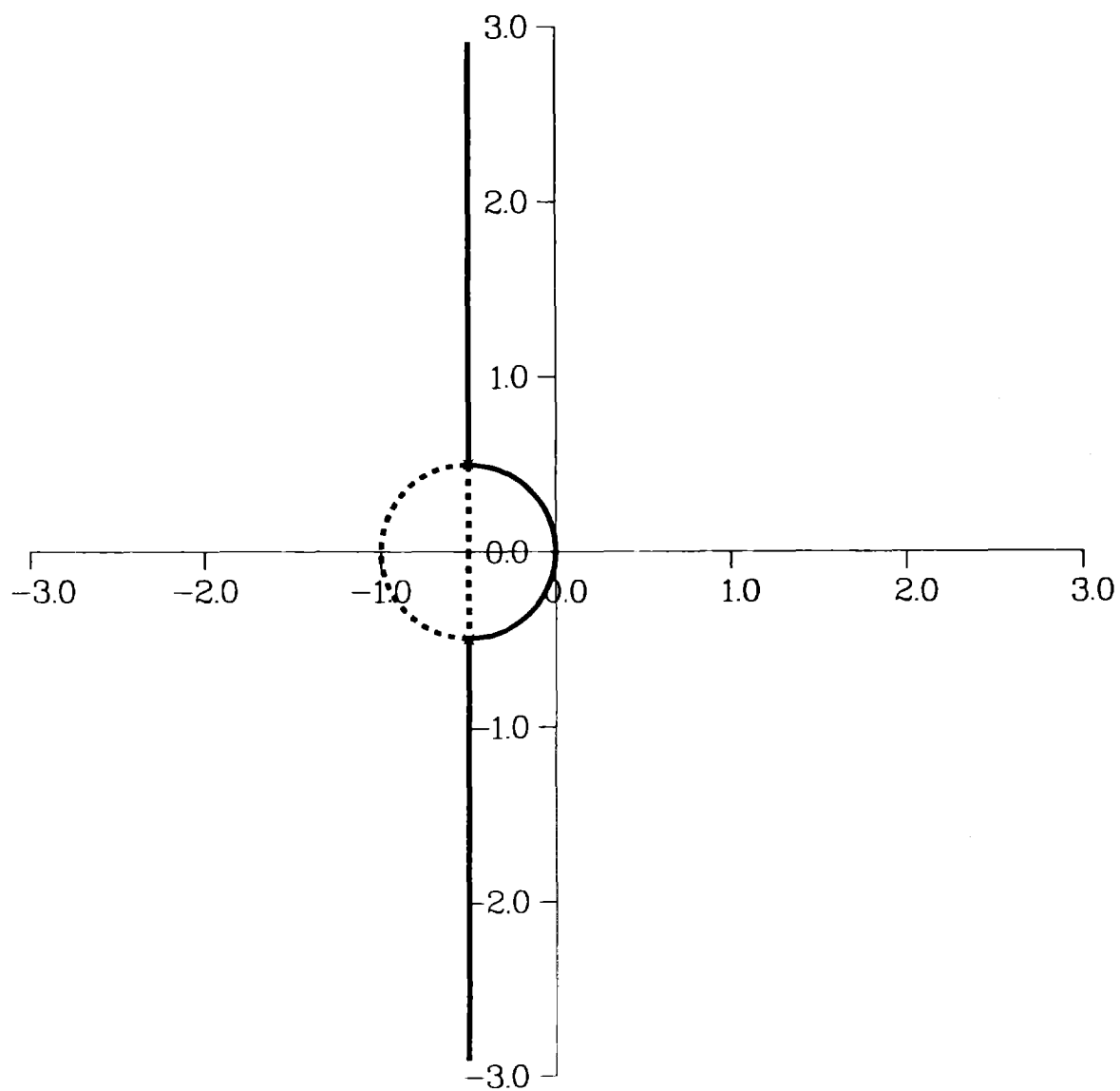


$$\alpha = 0.3$$

Fig. 7



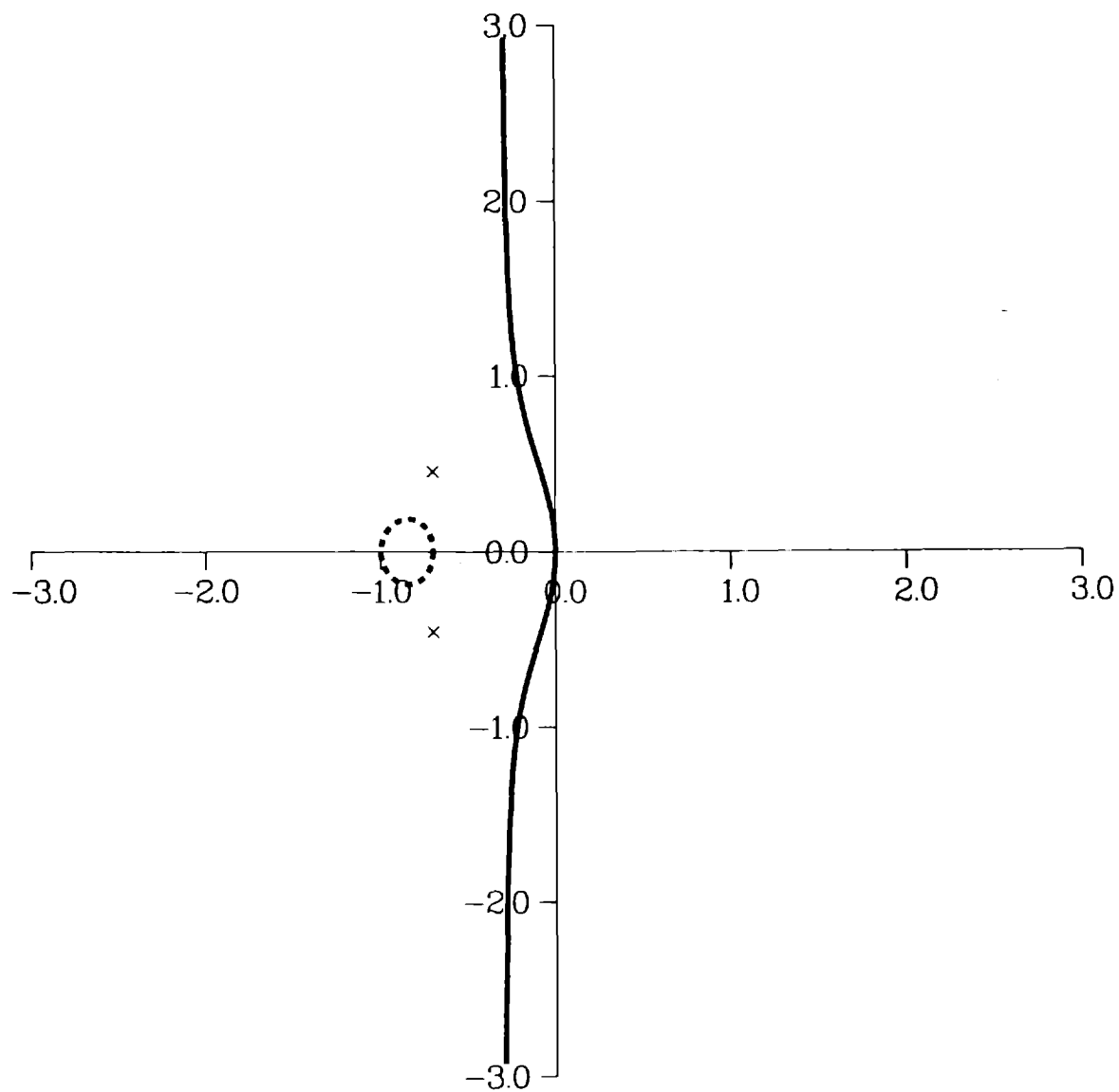
## Achenbach–Chao Solid



$$\alpha = 0.5$$

Fig. 8

## Achenbach–Chao Solid



$$\alpha = 0.7$$

Fig. 9

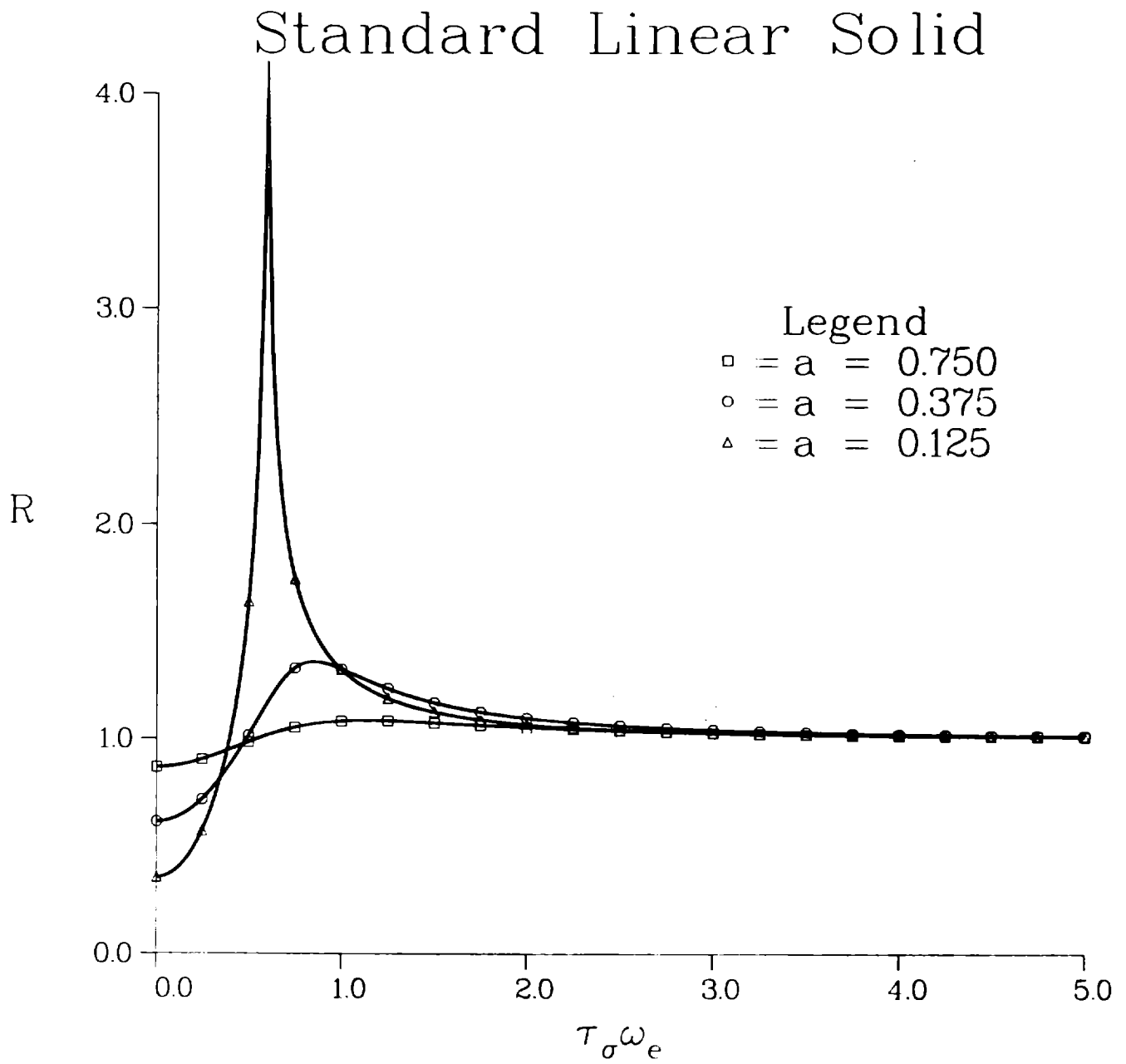


Fig. 10

# Achenbach–Chao Solid

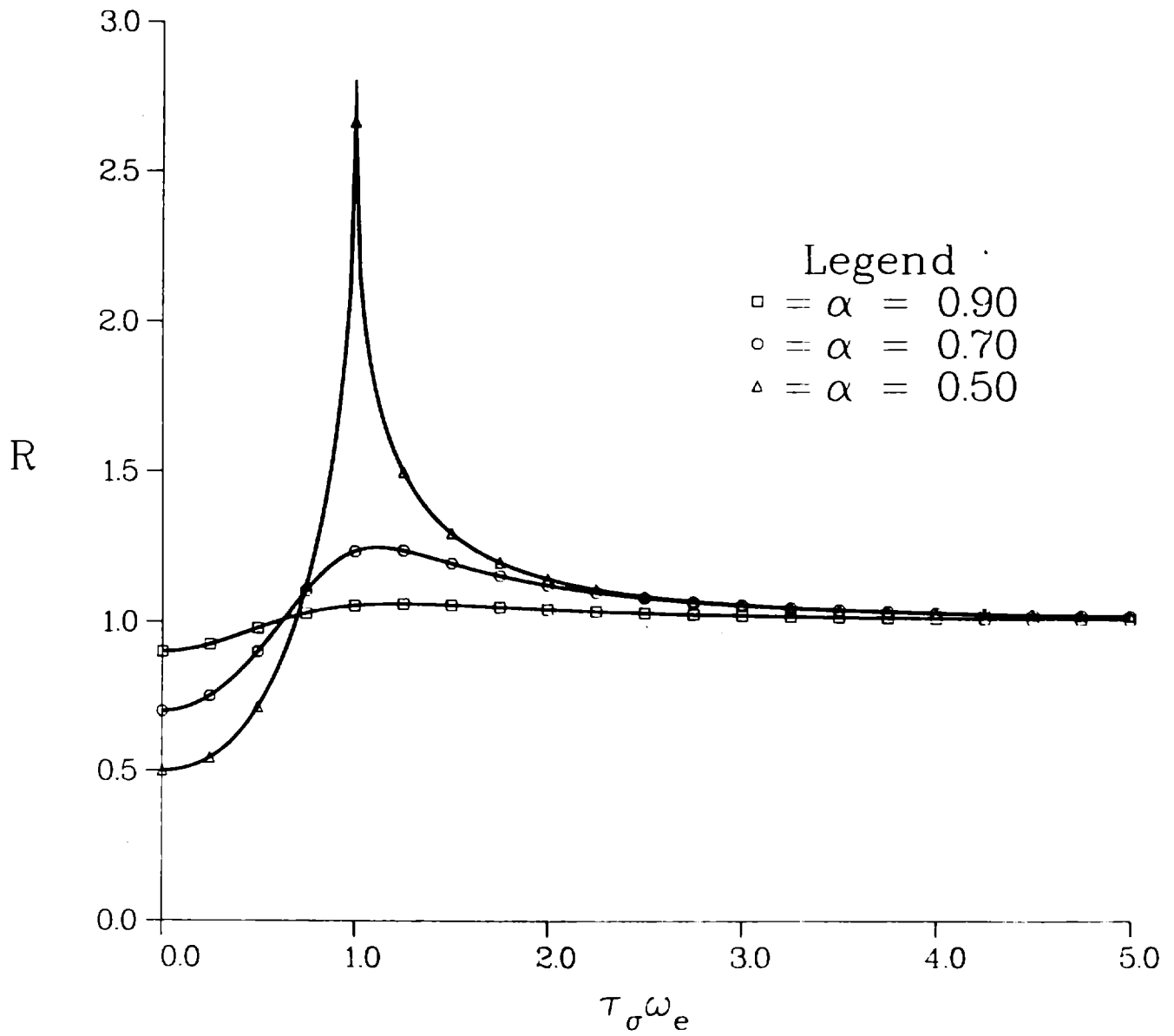


Fig. 11

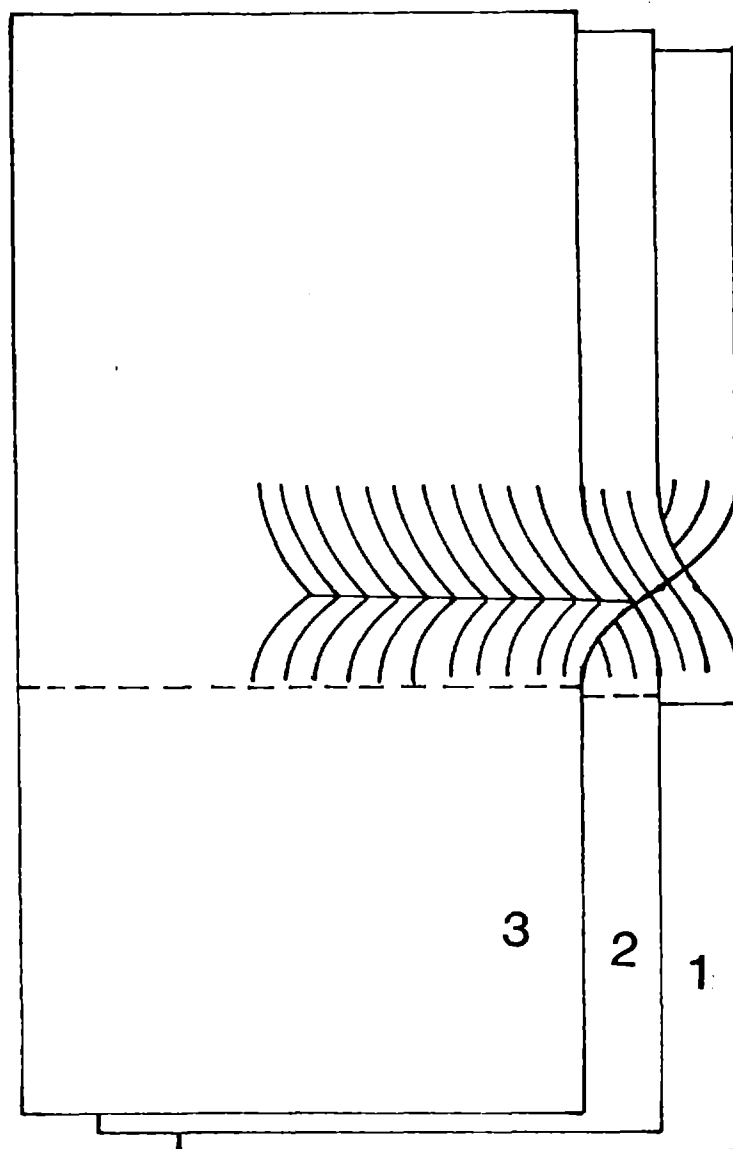


Fig. 12

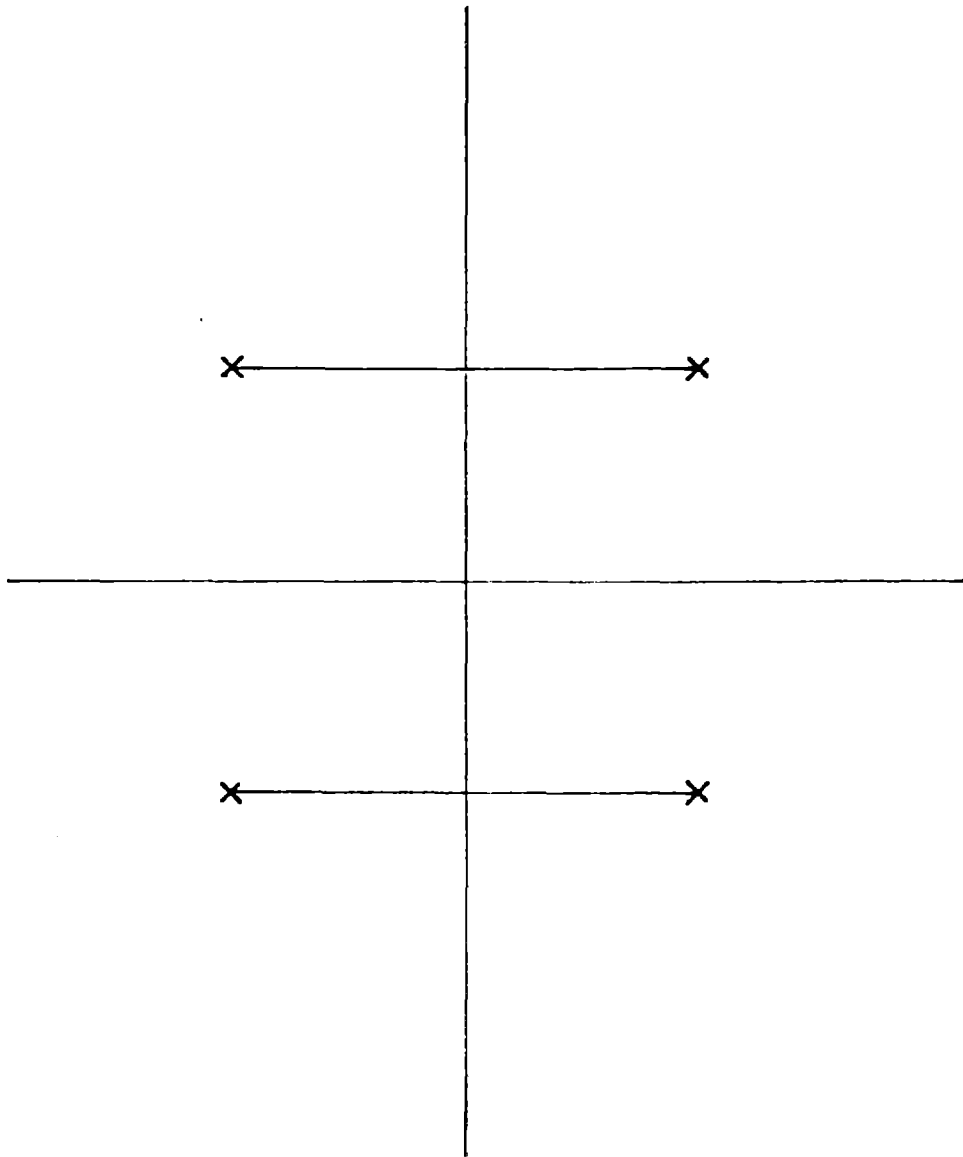
$\zeta$  - plane

Fig. 13

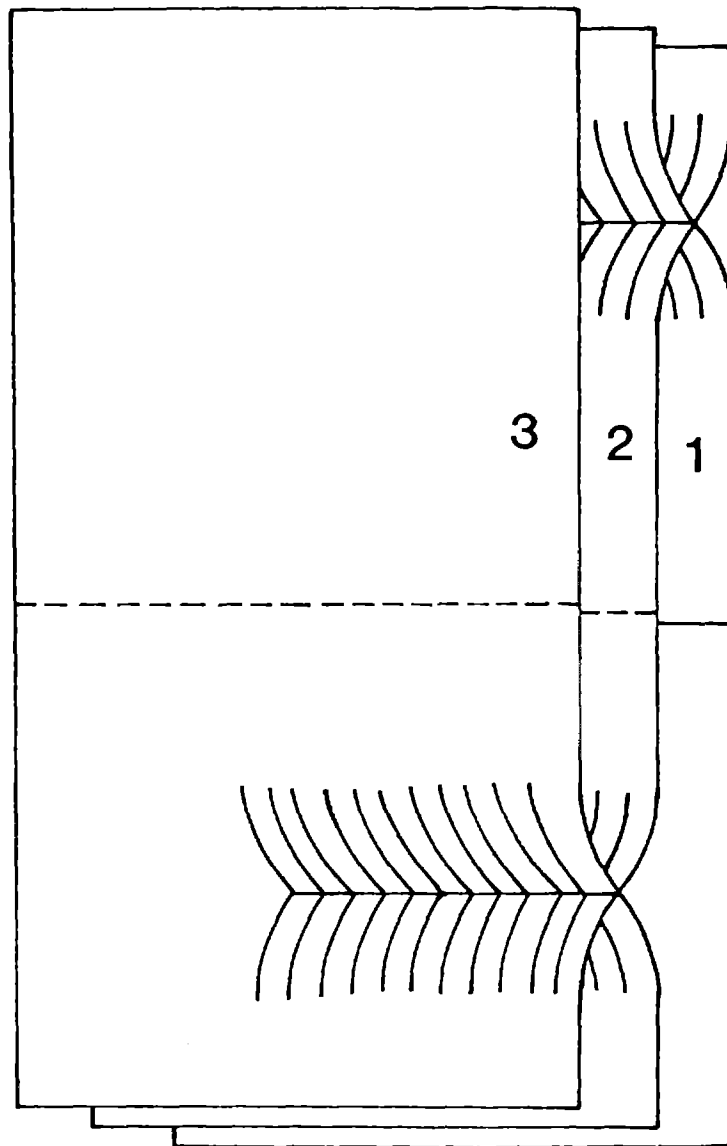


Fig. 14

## Streamlines

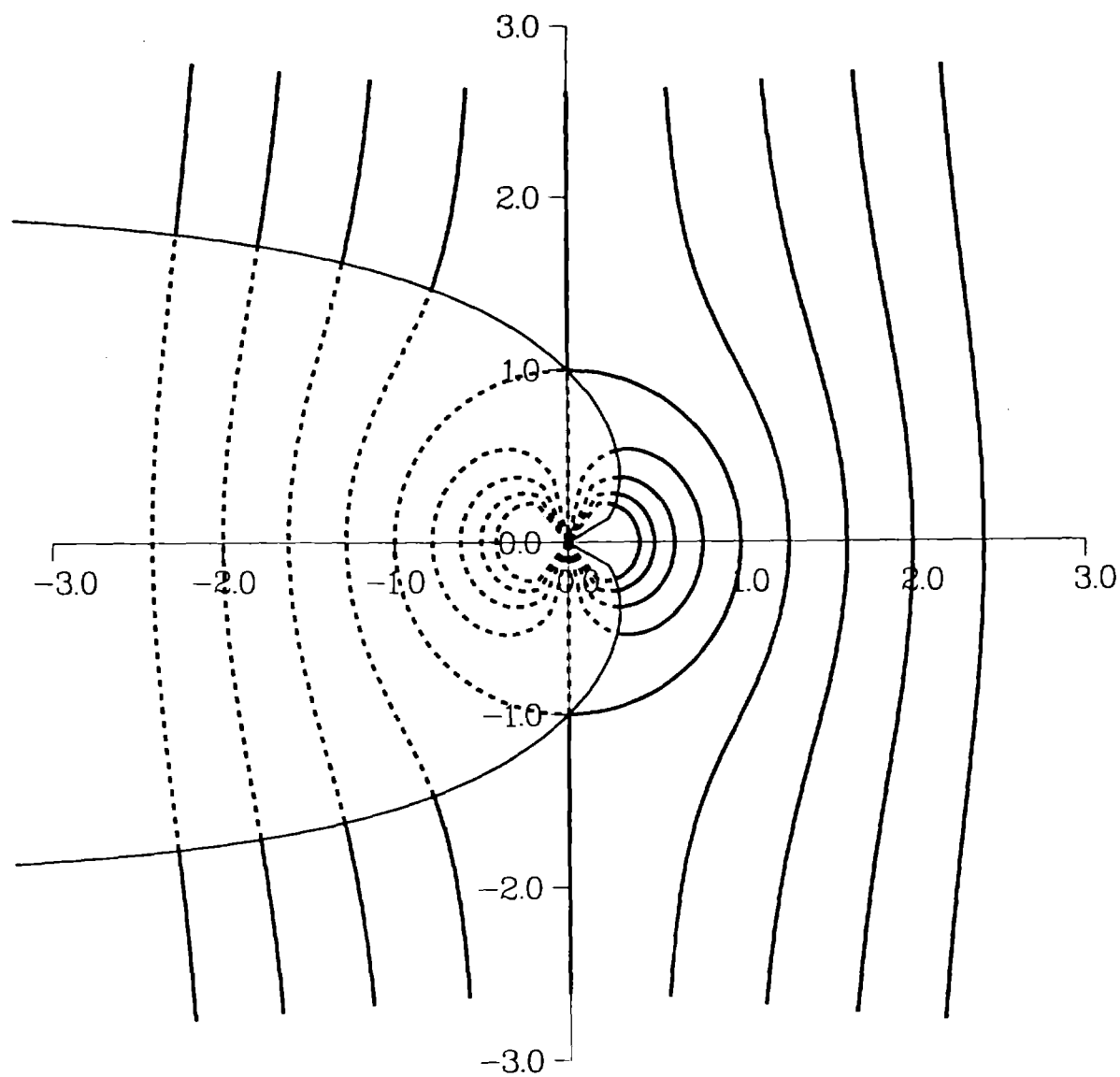


Fig. 15